MEASUREMENT OF THE FLAVOR ASYMMETRY IN THE NUCLEON SEA

A Dissertation

by

ERIC ANDREW HAWKER

Submitted to the Office of Graduate Studies of
Texas A&M University
in partial fulfillment of the requirements for the degree of

DOCTOR OF PHILOSOPHY

August 1998

Major Subject: Physics

MEASUREMENT OF THE FLAVOR

ASYMMETRY IN THE NUCLEON SEA

A Dissertation

by

ERIC ANDREW HAWKER

Submitted to Texas A&M University
in partial fulfillment of the requirements
for the degree of

DOCTOR OF PHILOSOPHY

Approved as to style and content by:

Robert E. Tribble
(Chair of Committee)

Carl A. Gagliardi
(Member)

Siu A. Chin
(Member)

Sherry J. Yennello
(Member)

Thomas W. Adair III
(Head of Department)

August 1998

Major Subject: Physics

ABSTRACT

Measurement of the Flavor

Asymmetry in the Nucleon Sea. (August 1998)

Eric Andrew Hawker, B.S., University of Illinois

Chair of Advisory Committee: Dr. Robert E. Tribble

A precise measurement made by Fermilab experiment E866 of the ratio of Drell-Yan yields from an 800 GeV/c proton beam incident on hydrogen and deuterium targets is reported. From this ratio of yields the asymmetry between anti-down and anti-up quark distributions in the nucleon is determined over a wide range in Bjorken-x. The x dependence of the ratio of $\bar{d}(x)$ to $\bar{u}(x)$ quarks shows a substantial excess of $\bar{d}(x)$ with respect to $\bar{u}(x)$ for $x < 0.25$. For $x > 0.25$ the data show the $\bar{d}(x)$ to $\bar{u}(x)$ ratio to be much closer to unity. Predictions made by current nucleon structure parametrizations are shown to be in reasonable agreement with the measured asymmetry results below an x of 0.15, but are in sharp disagreement with the results at values of x higher than 0.2. These very same results and issues are discussed in brief in a recent paper [The E866 Collaboration, E. A. Hawker *et al.*, Phys. Rev. Lett. **80**, 3715 (1998)]. The asymmetry measurements are also shown to be able to support or reject several current theoretical models which aim to describe the nucleon sea as arising from nonperturbative QCD processes.

To my wife Jennifer, and my parents Mary and Fred.

ACKNOWLEDGMENTS

I feel truly honored and fortunate to have been a member of the E866 Collaboration for the past five years. I would like to thank all of them for their continual help, patience, support, and friendship. Without their hard work, this experiment, let alone this dissertation, would never have been successful.

The E866 Collaboration

T.C. Awes, M.E. Beddo, C.N. Brown, J.D. Bush, T.A. Carey,
T.H. Chang, W.E. Cooper, C.A. Gagliardi, G.T. Garvey, D.F. Geesaman,
E.A. Hawker, X.C. He, L.D. Isenhower, S.B. Kaufman, D.M. Kaplan,
P.N. Kirk, D.D. Koetke, G. Kyle, D.M. Lee, W.M. Lee, M.J. Leitch,
N. Makins, P.L. McGaughey, J.M. Moss, B.A. Mueller, P.M. Nord,
B.K. Park, V. Papavassiliou, J.C. Peng, G. Petitt, P.E. Reimer,
M.E. Sadler, J. Selden, P.W. Stankus, W.E. Sondheim, T.N. Thompson,
R.S. Towell, R.E. Tribble, M.A. Vasiliev, Y.C. Wang, Z.F. Wang,
J.C. Webb, J.L. Willis, D.K. Wise, and G.R.Young

I would like to especially thank Bob Tribble and Carl Gagliardi for their unending help and patience in explaining things to me over the years; I will always value their advice (and thanks for sending me to France!). They were the first to begin teaching me what a high precision experiment in high energy physics was all about. My education was continued, when I came to Fermilab, by Chuck Brown, Pat McGaughey, and the many others who took the time to teach me and answer my questions about all sorts of different aspects of experimental high energy physics. The friendship of other graduate students on the experiment, Rusty, Jason, Bill, and Ting, also made life outside of physics enjoyable. Good luck to all of you in getting out of graduate school soon!

And most importantly, none of this would have been possible for me without the love, encouragement, and support of my parents, my wife, and the rest of my family and friends.

TABLE OF CONTENTS

CHAPTER Page

LIST OF TABLES

LIST OF FIGURES

FIGURE Page

CHAPTER I

INTRODUCTION, THEORY, AND MOTIVATION

A. Introduction

Stable matter on Earth is made up of protons, neutrons, and electrons. Electrons appear to be fundamental particles; they are point-like with no discernable structure. Protons and neutrons (generically called nucleons), on the other hand, are not fundamental. There are two types of particles present in a nucleon, quarks and gluons, both of which appear to be fundamental in nature. Exactly how quarks and gluons form the structure of a nucleon is quite complex, and not yet completely understood. What is known is as follows. A nucleon is made up of three valence quarks held together in a bound state by the strong force mediated by gluons. Also present is a "background sea" of quark-antiquark ($q\bar{q}$) pairs.

Quantum chromodynamics (QCD) is a field theory which describes the strong interactions of quarks and gluons. At large four momentum transfers (above 1 or 2 GeV), perturbative methods can be used with QCD to calculate the results of an interaction. At lower momentum transfers non-perturbative QCD must be used in order to make any predictions about the results of the interaction. However, non-perturbative QCD calculations are very difficult and limited in what they are able to predict.

It is possible to understand aspects of $q\bar{q}$ pair creation within a nucleon through perturbative processes. Gluons can "pair produce" a virtual quark-antiquark pair; after a short time the pair annihilate to form another gluon. However, perturbative processes can not explain the existence or the dynamics of the entire quark sea of

The journal model is Physical Review D.

the nucleon. As early as 1976 it had been pointed out by Field and Feynman [1] that the Pauli exclusion principle could cause an asymmetry between the production of $u\bar{u}$ pairs and $d\bar{d}$ pairs. In the proton, where there are one d and two u valence quarks, there is one more state available for a $d\bar{d}$ pair than a $u\bar{u}$ pair. So by this argument, there should be a very slight excess of $d\bar{d}$ pairs with respect to $u\bar{u}$ pairs in the proton. In contrast, since down quarks have a slightly greater mass than up quarks, sea quark production processes should slightly favor the creation of $u\bar{u}$ pairs over $d\bar{d}$ pairs. With the exception of these two arguments, there were no compelling reasons for a flavor asymmetry of any great size until recently, and so it was generally accepted that there was an approximate up down flavor symmetry in the nucleon sea.

B. Deep inelastic scattering

One method used to probe the structure of the nucleon is to inelastically scatter a high energy charged lepton off of a target nucleon. In this process, known as deep inelastic scattering (DIS), the lepton scatters off a single quark in the target nucleon by way of an exchange of a high energy virtual photon. The resulting measured differential cross section can be parameterized in terms of two structure functions $F_1(x, Q^2)$ and $F_2(x, Q^2)$;

$$\frac{d\sigma}{dE'd\Omega} = \frac{\alpha^2}{4E'\sin^4\frac{\theta}{2}}\left[\frac{1}{\nu}F_2(x,Q^2)\cos^2\frac{\theta}{2} + \frac{1}{M}F_1(x,Q^2)\sin^2\frac{\theta}{2}\right], \qquad (1.1)$$

where α is the electromagnetic fine structure constant, E' is the final state energy of the scattered lepton, θ is the angle the lepton scatters through in the lab frame, ν is the energy lost by the scattered lepton in the lab frame, and M is the mass of the target nucleon. These structure functions are, in turn, functions of Bjorken-x, a dimensionless scaling variable that at high energies represents the fraction of the nucleon's longitudinal momentum that is carried by a quark or gluon, and of Q^2, the four momentum squared of the virtual photon exchanged in the process. In the parton model of the nucleon, the $F_1(x,Q^2)$ and $F_2(x,Q^2)$ structure functions can be expressed as linear combinations of the probability distribution functions of each flavor of quark. Probability (or parton) distribution functions (PDF's) describe the underlying structure of the nucleon in terms of the probability that a specific type of parton exists with a momentum fraction between x and $x+dx$, when measured with a four momentum transfer of Q^2.

$$F_1(x,Q^2) = \sum_i \frac{e_i^2}{2} q_i(x,Q^2) \tag{1.2}$$

$$F_2(x,Q^2) = \sum_i e_i^2 x q_i(x,Q^2) \tag{1.3}$$

In these equations $q_i(x,Q^2)$ is the probability distribution function for the ith quark or antiquark flavor, and e_i^2 is its charge squared. At a constant value of x, the F_2 structure functions as well as the PDF's vary slowly with respect to changes in Q^2. Because of the weak dependence these functions have on Q^2, I will ignore this dependence for now. I will also define the probability distribution functions as a function of x for the up, down, anti-up, and anti-down quark flavors as $u(x)$, $d(x)$, $\bar{u}(x)$, and $\bar{d}(x)$ respectively. Since the proton has two valence up quarks and one valence down quark, the valence distributions, $d_v(x)$ and $u_v(x)$, must obey the following sum rules

$$\int_0^1 u_v(x)dx = \int_0^1 [u(x) - \bar{u}(x)]\, dx = 2 \tag{1.4}$$

$$\int_0^1 d_v(x)dx = \int_0^1 \left[d(x) - \bar{d}(x)\right] dx = 1. \tag{1.5}$$

Due to their nearly equal mass, there is an approximate symmetry between the proton and neutron. The (almost) conserved quantity in this symmetry is called isospin. Isospin is very similar to normal spin in quantum mechanics. The neutron and proton isospin states form a doublet in isospin space, much like the two spin states of the electron form a doublet in spin space. Although isospin was originally introduced to explain a symmetry between protons and neutrons in a nuclear context, the symmetry has since been extended to the underlying quarks where the up and down quarks, due to their nearly equal mass, are also considered to form an isospin doublet. A special case of this symmetry, called charge symmetry, occurs when an entire system of particles undergoes a 180° rotation in isospin space. As an example of this, consider a proton - a large system of quarks, anti-quarks, and gluons - going through a 180° rotation in isospin space and becoming a neutron. According to charge symmetry all particles in the system must go through this rotation, so all of the up quarks in the proton would rotate into down quarks in the neutron, and all of the down quarks in the proton would rotate into up quarks in the neutron. Therefore, according to charge symmetry

$$u^p(x) = d^n(x) \tag{1.6}$$

$$d^p(x) = u^n(x) \tag{1.7}$$

$$\bar{u}^p(x) = \bar{d}^n(x) \tag{1.8}$$

$$\bar{d}^p(x) = \bar{u}^n(x), \tag{1.9}$$

where the n and p superscripts denote a neutron or proton PDF respectively.

1. *Gottfried sum rule*

In the late 60's, Gottfried [2] developed a method to relate the DIS structure function F_2 to the electric and magnetic form factors which describe the charge distribution within the nucleon. Since then this method has been modified to examine the difference of the proton and neutron structure functions. The Gottfried Sum is defined as

$$I_{GS} = \int_0^1 [F_2^p(x) - F_2^n(x)] \frac{dx}{x}. \tag{1.10}$$

If the $F_2(x)$ structure functions are re-written in terms of the appropriate PDF's, then Eq. 1.10 becomes

$$\begin{aligned} I_{GS} &= \int_0^1 [F_2^p(x) - F_2^n(x)] \frac{dx}{x} \\ &= \int_0^1 \Bigg\{ \left[\frac{4}{9}\left(u^p(x) + \bar{u}^p(x)\right) + \frac{1}{9}\left(d^p(x) + \bar{d}^p(x)\right)\right] \\ &\quad - \left[\frac{4}{9}\left(u^n(x) + \bar{u}^n(x)\right) + \frac{1}{9}\left(d^n(x) + \bar{d}^n(x)\right)\right]\Bigg\} dx, \end{aligned} \tag{1.11}$$

where I have assumed that the distribution functions for the heavier quarks are the same in both the proton and neutron, and so cancel out. Charge symmetry can be used to write Eq. 1.11 in terms of proton PDF's only as

$$I_{GS} = \int_0^1 \frac{1}{3}\left[u(x) - d(x) + \bar{u}(x) - \bar{d}(x)\right] dx, \tag{1.12}$$

where the p superscript has now been dropped. This equation can be further simplified using the sum rules shown in Eq. 1.4 and Eq. 1.5 to arrive at,

$$I_{GS} = \frac{1}{3} - \frac{2}{3}\int_0^1 \left[\bar{d}(x) - \bar{u}(x)\right] dx. \tag{1.13}$$

If the up and down sea quark distributions are the same, the right side of Eq. 1.13 simply becomes $\frac{1}{3}$. This result is referred to as the Gottfried Sum Rule (GSR).

2. *The New Muon Collaboration experiment*

The New Muon Collaboration (NMC) [3] performed a DIS experiment using a beam of high energy muons incident on hydrogen and deuterium targets. They were able to measure the F_2 structure functions of both hydrogen and deuterium, and extract from their data

$$\int_{0.004}^{0.8} [F_2^p(x) \; - \; F_2^n(x)] \frac{dx}{x} \; = \; 0.221 \pm 0.008(stat) \pm 0.019(syst). \qquad (1.14)$$

When NMC extrapolated their results to the limits of Bjorken-x, they determined

$$\int_0^1 [F_2^p(x) \; - \; F_2^n(x)] \frac{dx}{x} \; = \; 0.235 \pm 0.026, \qquad (1.15)$$

which clearly deviates from $\frac{1}{3}$.

There are several possible reasons why NMC has seen a violation of the Gottfried Sum Rule. One possible reason for the GSR violation could be that the extrapolation done by NMC to find the GSR integral over the full range of x was incorrect. The GSR is valid, in the limit of a flavor symmetric nucleon sea, only if the integral shown in Eq. 1.10 is evaluated over the full range of x. Since experimentally it is very difficult to make measurements down to $x = 0$, an extrapolation must be done if experimental data are to be compared to the GSR. The $1/x$ dependence of Eq. 1.10 causes the GSR to be highly sensitive to F_2 at low x, so any error in the NMC extrapolation of the structure functions could explain the NMC results and still have the GSR be valid.

Part of the difficulty of measuring the GSR integrand at low x is in the method used to determine F_2^n. Because it is not possible to use a pure neutron target, F_2^n must be extracted from the F_2 structure function of a nucleus such as a deuteron. Nuclear effects, such as nuclear shadowing [4], can make the measurement of F_2^n increasingly more difficult as x gets smaller. Fermilab experiment E665 [5] also performed a DIS experiment with a beam of high energy muons incident on hydrogen and deuterium targets. While E665 did not extract I_{GS} from their data, they did compare their extracted values of the ratio F_2^n/F_2^p to the values NMC determined for the same quantity. E665 found their results to be consistent with the results from NMC in the range of x where both experiments took data. However, E665 was able to take data at much lower values of x than NMC (down to 10^{-6}). In the range of $x < 0.01$, E665 found the ratio F_2^n/F_2^p was nearly constant at $0.935 \pm .008$, instead of the expected value of unity. This may be an indication that nuclear effects in deuterium affected the measurement of F_2^n at low x.

Although we know charge symmetry is not exact, when Eq. 1.10 is rewritten as Eq. 1.12, charge symmetry is assumed to be a "good" symmetry. This "false" assumption could be another reason for the GSR violation found by NMC. However this is very unlikely, since there is a great deal of evidence [6] showing the violation of charge symmetry to be very small. Charge symmetry would have to be broken on a much larger scale if it were to account for NMC's results.

The simplest reason for the observed GSR violation is a flavor asymmetry in the proton sea in the form of an excess of down sea quarks relative to up sea quarks. To date this has been the most widely accepted explanation of the NMC result [7].

C. Drell-Yan

The nucleon sea can be probed by using processes other than DIS. In a Drell-Yan interaction [8], a quark and antiquark annihilate into a virtual photon, which then decays into a pair of oppositely charged leptons, as shown in Fig. 1. The proton-nucleon cross section for the Drell-Yan process to leading order in α^2, as a function of the x of the initial quark (q) and antiquark ($\bar{q}$), is

$$\frac{d\sigma^{pN}}{dx_1 dx_2} = \frac{4\pi\alpha^2}{9x_1x_2s}\sum_i e_i^2\left[q_{i1}(x_1)\bar{q}_{i2}(x_2) + q_{i2}(x_2)\bar{q}_{i1}(x_1)\right], \tag{1.16}$$

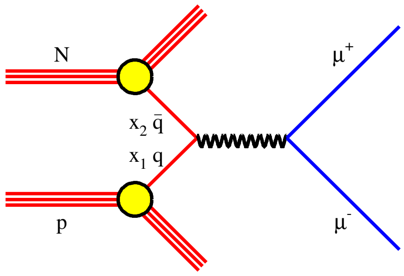

FIG. 1. A diagram of the leading order Drell-Yan process.

where the sum is over all quark flavors, e is the charge of that flavor of quark, and the subscripts 1 and 2 indicate a beam or target quark respectively. Two kinematic variables often used in describing Drell-Yan events are x_F (called x Feynman) and the dilepton mass M; they are defined as

$$x_F = p_{||}^{\gamma}/p^{\gamma,max} \approx x_1 - x_2 \tag{1.17}$$

$$M^2 = Q^2 \approx x_1 x_2 s, \tag{1.18}$$

where $p_{||}^{\gamma}$ is the center of mass longitudinal momentum of the virtual photon, and $p^{\gamma,max}$ is its maximum possible value. The variable s is defined as the total four momentum squared of the initial nucleons

$$s = (p_p + p_N)^2. \tag{1.19}$$

While it is obvious that the Drell-Yan process is sensitive to sea quark distributions, Ellis and Stirling [9] were the first to suggest using this process as a method to investigate the sea quark flavor asymmetry in the nucleon.

1. *The NA51 experiment*

The NA51 experiment [10] used the 450 GeV/c ($\sqrt{s} = 29$ GeV) proton beam from the CERN Synchrotron Proton Source and the NA10 spectrometer to compare the Drell-Yan dimuon yields from hydrogen and deuterium targets. NA51 was able to measure the ratio of cross sections σ^{pp}/σ^{pd}, where the pp and pd superscripts indicate the proton-proton and the proton-deuteron Drell-Yan cross sections respectively. From this ratio NA51 was able to extract a measurement of the up-down flavor asymmetry of the proton sea. As an example of how this extraction was done, consider the case of Drell-Yan interactions with $x_F = 0$. In this simplified analysis, which is a reasonable characterization of the the data taken by NA51, the Drell-Yan cross sections can be approximately written as

$$\sigma^{pp}(x) \propto \frac{8}{9}u(x)\bar{u}(x) + \frac{2}{9}d(x)\bar{d}(x) \tag{1.20}$$

$$\begin{aligned} \sigma^{pd}(x) &\approx \sigma^{pp} + \sigma^{pn} \\ &\propto \left[\frac{8}{9}u(x)\bar{u}(x) + \frac{2}{9}d(x)\bar{d}(x)\right] + \left[\frac{5}{9}u(x)\bar{d}(x) + \frac{5}{9}d(x)\bar{u}(x)\right]. \end{aligned} \tag{1.21}$$

Contributions to the cross sections from heavier quark terms have been ignored, charge symmetry has been used to express the proton deuteron cross section in terms of only proton PDF's, and shadowing has been neglected. The ratio of the cross sections can then be written as

$$\left.\frac{\sigma^{pd}}{\sigma^{pp}}\right|_{x_1=x_2} = \frac{8 + 5(\bar{d}/\bar{u}) + (d/u)(5 + 2(\bar{d}/\bar{u}))}{8 + 2(d/u)(\bar{d}/\bar{u})}, \tag{1.22}$$

where the notation showing the x dependence has been dropped. It is now simple to solve for $\bar{d}/\bar{u}$,

$$\frac{\bar{d}}{\bar{u}} = \frac{8\left[(\sigma^{pd}/\sigma^{pp}) - 1\right] - 5(d/u)}{5 + \left[1 - (\sigma^{pd}/\sigma^{pp})\right]2(d/u)}. \tag{1.23}$$

Because x_F is not exactly zero for all of their data, NA51 performed a more extensive and complete analysis, from which they were able to report

$$\left.\frac{\bar{u}}{\bar{d}}\right|_{<x>=0.18} = 0.51 \pm 0.04(stat) \pm 0.05(syst). \tag{1.24}$$

This result, even though it requires charge symmetry to be invoked, confirms the previous conclusion that the quark sea in the nucleon is asymmetric with respect to the up and down quark flavors. Unlike the NMC result, NA51's extraction of $\bar{u}/\bar{d}$ is insensitive to nuclear effects, since experiments have not seen evidence of nuclear effects in Drell-Yan interactions in the x region where NA51 took data [11].

However, there were two major drawbacks to the NA51 experiment. First, NA51 was able to collect only a small sample of useful Drell-Yan events from their hydrogen and deuterium targets. Less than 6000 events total were used in the $\bar{u}/\bar{d}$ determination. This is the reason why NA51 presented a flavor asymmetry for only a single average value of $< x >= 0.18$. Second, as alluded to previously, the spectrometer used by the NA51 collaboration had a narrow x_F acceptance centered at $x_F = 0$. The momentum distributions for the quark sea have a maximum value at $x = 0$ and decrease exponentially as x increases, as shown in Fig. 2. Valence quarks, on the other hand, have momentum distributions with a minimum at $x = 0$ and increase to a maximum between $x = 0.05$ and $x = 0.2$ before decreasing exponentially as x increases, as also shown in Fig. 2. In a Drell-Yan interaction, if x_F is large ($x_F > 0.3$) there is a high probability that the parton in the target nucleus, with momentum fraction x_2, is the antiquark, and the parton in the beam proton, with momentum fraction x_1, is the quark. Since the antiquark must have originated in the nucleon sea, a Drell-Yan event at large x_F allows us to make an approximate measurement of the nucleon sea at x_2. On the other hand, if $x_F \approx 0$, as it is for most of the NA51 data, then σ^{pd}/σ^{pp} is less sensitive to an asymmetry in the target nucleon sea.

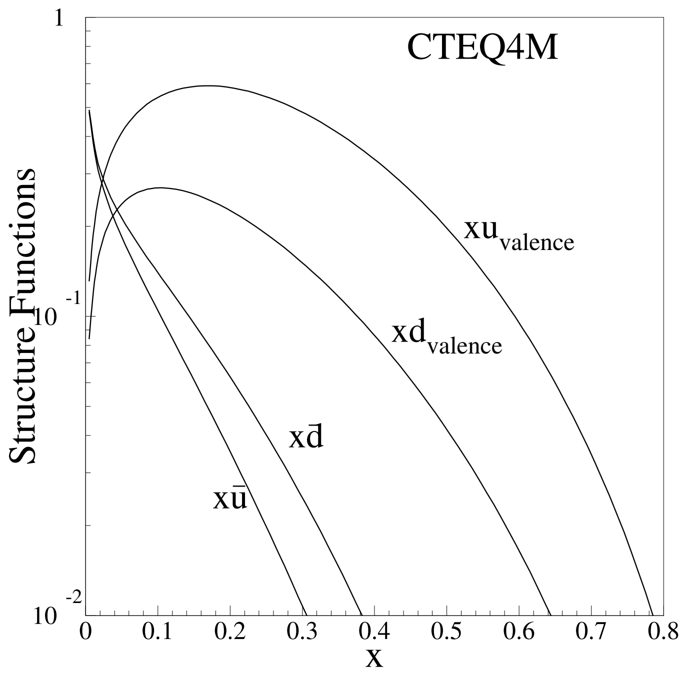

FIG. 2. A typical momentum distribution set at a Q of 7 GeV [12].

2. *Fermilab experiment E866*

In this dissertation, I report on a measurement of the flavor asymmetry in the nucleon sea extracted from $\approx 40\%$ of the data collected by Fermilab E866. Experiment E866 used the Drell-Yan process to study the flavor asymmetry in the nucleon sea, much like NA51 did. However, E866 was able to acquire data at much larger values of x_F than NA51 was able to achieve. In the large x_F limit, if it is assumed the antiquark is always from the target nucleus, then the Drell-Yan cross sections can be simplified to

$$\sigma^{pp}(x) \propto \frac{4}{9}u_1\bar{u}_2 + \frac{1}{9}d_1\bar{d}_2 \tag{1.25}$$

$$\begin{aligned}\sigma^{pd}(x) \approx\ & \sigma^{pp} + \sigma^{pn} \\ \propto\ & \left[\frac{4}{9}u_1\bar{u}_2 + \frac{1}{9}d_1\bar{d}_2\right] \ + \ \left[\frac{4}{9}u_1\bar{d}_2 + \frac{1}{9}d_1\bar{u}_2\right],\end{aligned} \tag{1.26}$$

where the same assumptions have been made as in Eq. 1.20 and Eq. 1.21, and the subscripts 1 and 2 indicate the PDF is a function of x_1 or x_2 respectively. The ratio of these cross sections is then

$$\left.\frac{\sigma^{pd}}{\sigma^{pp}}\right|_{x_1>>x_2} \approx \frac{1 \ + \ d_1/4u_1}{1 \ + \ (d_1/4u_1)\cdot(\bar{d}_2/\bar{u}_2)}\left(1 \ + \ \frac{\bar{d}_2}{\bar{u}_2}\right). \tag{1.27}$$

Comparing Eq. 1.22 and Eq. 1.27, it can be seen that the cross section ratio in the large x_F case is more sensitive to $\bar{d}/\bar{u}$ than the small x_F case.

In addition to the increased sensitivity to the flavor asymmetry, E866 was also able to make a more precise measurement of the cross section ratio over a larger range of x than NA51 was able to accomplish. This was because E866 recorded well over 50 times more Drell-Yan events than NA51. The higher sensitivity along with the higher statistics has allowed E866 to report a precise determination of the flavor asymmetry in the nucleon sea over a wide range in x.

Since NMC first reported their result, there have been many models created to try to explain how a flavor asymmetry can be produced in the quark sea of the nucleon. Meson cloud, chiral-quark, and instanton models are all able to predict an x dependence of this asymmetry. The x dependence of the asymmetry measured by E866 will help to support or reject many of these models.

This dissertation describes the apparatus, experimental procedures, analysis of the data, and the calculation of $\sigma^{pd}/2\sigma^{pp}$ for E866. The methods used to extract the quantities $\bar{d}/\bar{u}$ and $\bar{d} - \bar{u}$ as functions of x from the cross section ratios are discussed, and the results are compared to several models.

CHAPTER II

THE EXPERIMENTAL APPARATUS

The basic experimental goal of Fermilab E866 was the detection of the two oppositely charged muons from the Drell-Yan interactions produced by a high energy beam of protons hitting a liquid hydrogen or deuterium target. E866 was the fourth experiment to use the spectrometer [13], shown in Fig. 3, located in the Meson East experimental hall at Fermilab. This spectrometer can detect beam-target interaction events which produce two oppositely charged muons (referred to as dimuon events from now on) and measure the kinematic properties of these events. The spectrometer primarily consisted of three large dipole magnets and four detector stations, with each station containing wire chambers and scintillation detectors. The four detector stations and the SM3 magnet were used to measure the momentum and trajectory of muons traveling through the spectrometer. From these measurements, the four momentum each muon had at the target was able to be reconstructed, which allowed the x_F and dimuon mass for each event to be calculated. With the targets positioned as shown in Fig. 3, the spectrometer primarily accepted dimuon events with large x_F values. The strengths of the fields in the SM0 and SM12 magnets determined the range of dimuon masses, and to second order the range of x_2 values, accepted by the spectrometer.

A thick hadron absorber wall was installed in SM12 for the experiment so that the spectrometer would only detect muons and not hadrons from beam-target interactions. Without the absorber wall E866 would have been forced to take data at a much lower rate. Several other changes were made to the spectrometer for this experiment. A larger set of drift chambers were constructed for the first detector station to increase the acceptance of the spectrometer. The trigger system was redesigned

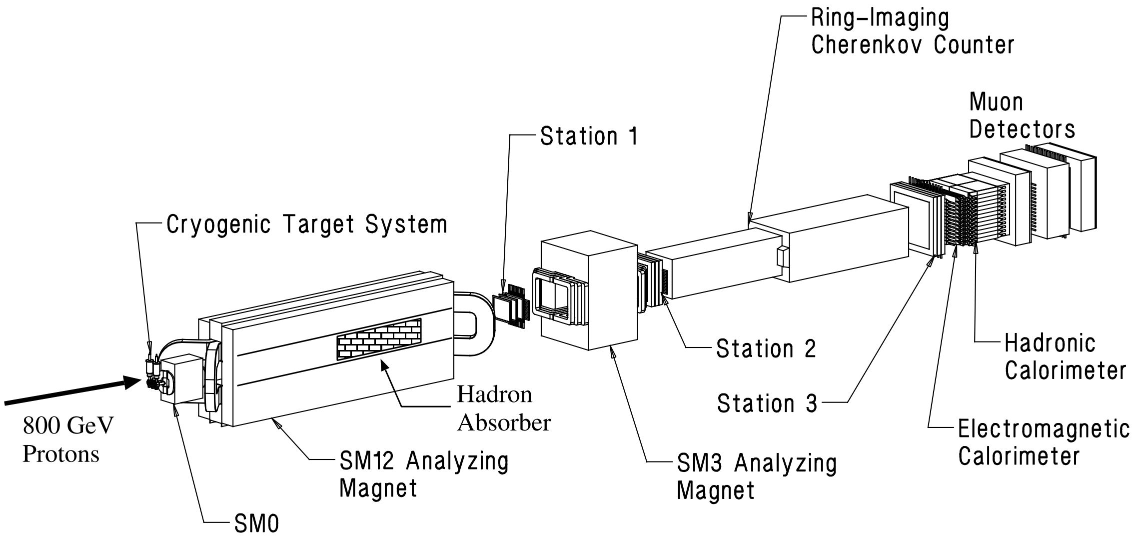

FIG. 3. The E866 spectrometer.

in order to increase its acceptance, flexibility and reliability. The data acquisition system was improved in order to combine both normalization and event information into the same data stream. Without this improvement the data acquisition system would have contributed to the overall systematic uncertainty of the experiment.

Section A of this chapter describes components of the spectrometer in approximately the same order as particles see them. Similarly, section B discusses the electronic systems of the spectrometer in roughly the same order as they process the detector information. To describe the experiment I will use a coordinate system with the z axis pointing in the direction the proton beam traveled, the y axis pointing up, and the x axis completing a right handed coordinate system.

A. The E866 spectrometer

1. *Beamline and targets*

E866 used an 800 GeV proton beam that was extracted from the Fermilab Tevatron accelerator. There were several beamline detectors used to monitor and record the size, position, and intensity of the beam. The beam intensity was monitored by the IC3 ion chamber, the SEM6 secondary emissions monitor, and a beam Cherenkov monitor. Both the size and the position of the beam were monitored by segmented wire ion chambers (SWICs), the most important of these being the ME6SWIC (the SWIC in Meson East enclosure six), which was positioned about 70 inches in front of the targets.

The Tevatron delivered beam for a 20 second "spill" once during every 60 second accelerator cycle. The beam during the spill was divided into "RF buckets" each ≈ 1 ns long, with ≈ 19 ns between beam buckets. This small scale beam structure was due to the Tevatron accelerating radio frequency (RF) of 53 MHz. A square wave signal at this frequency, called the RF clock, was used to synchronize the E866 electronics with the Tevatron beam cycle.

The targets used were 20 inch long, thin walled, cylindrical stainless steel flasks, each enclosed in an insulated vacuum jacket which had thin windows at both ends of the target flask. The targets contained either liquid hydrogen, liquid deuterium, or vacuum. The hydrogen and deuterium targets were 7% and 15% of a nuclear interaction length thick, respectively. The targets, along with the required cryogenic equipment, sat on a moveable platform which allowed the targets to be switched between beam spills. Both the temperature and the vapor pressure of the liquid targets were monitored as part of the control system for the target cryogenics. A relative measurement of the beam intensity hitting the target was made by the AMON and

WMON detectors. Both of these detectors were four element scintillator telescopes that looked at the targets through small holes in the very thick shielding in place around the target enclosure. These holes in the shielding were set at about 85° from the beam direction so that AMON and WMON would receive only a small fraction of the scattered particles produced by the beam hitting the target.

One way that the position of the target platform was monitored was by the number of particles seen by the AMON detector per unit beam intensity. When a denser target, such as deuterium, was in the beam, the particle rate per unit beam intensity seen by the AMON detector was higher than the rate per unit beam intensity seen when a lighter target, such as hydrogen, was in the beam. The target platform moved the targets into and out of the path of the beam over the course of a twelve spill long cycle. The hydrogen target was in the beam for five spills, followed by one spill with the empty target, then five spills with the deuterium target, and then again one spill with the empty target.

2. *Spectrometer magnets*

Immediately downstream of the targets was the 72 inch long SM0 dipole magnet. This magnet, as well as the SM12 and SM3 magnets, all produced horizontal magnetic fields in their apertures. The purpose of the SM0 and SM12 magnets was to collect and focus as many muons as possible into the detection region of the spectrometer. When run at its maximum current, the SM0 magnet caused a transverse momentum deflection of 0.94 GeV/c in the plus or minus y direction to the charged particles traveling through it. Filling the aperture of the SM0 magnet was a plastic bag which was kept full of helium gas. This and other helium gas bags in the spectrometer were used to minimize the amount of material muons would interact with other than the material in the SM12 absorber wall. After the SM0 magnet was the much larger 567 inch long SM12 dipole magnet. At a maximum current of 4000 amperes, this magnet produced a transverse momentum deflection of 7 GeV/c in the tracks of the charged particles which traveled completely through it. The remainder of the beam which did not interact in the target interacted in a 132 inch long solid copper beam dump which was located 68 inches downstream from the front of SM12. The beam dump was over 22 nuclear interaction lengths and over 233 radiation lengths thick.

A huge flux of high energy particles was created from both beam-target and beam-dump interactions. Out of these large numbers of particles, the only ones that were of interest were the muons that originated from the target. An absorber wall was used to filter out all particles except muons (and neutrinos). This was possible because, unlike the many hadrons produced by beam interactions, muons are not involved in strong force interactions. In addition high energy muons lose less energy in electromagnetic interactions than high energy electrons or photons. By filtering out all other particles except for muons (and neutrinos), E866 was able to take data with a high beam intensity without having to worry about radiation safety concerns or the loss of tracking efficiency caused by too many particles going through the spectrometer.

The absorber wall (called the hadron absorber in Fig. 3) was over 13 nuclear interaction lengths and over 60 radiation lengths thick. It was located directly behind the beam dump and completely filled the SM12 magnet aperture in the x and y directions. This wall was comprised of several different materials, stacked in layers in the z direction. The absorber wall was made of one 24 inch section of copper, three 27 inch sections of carbon graphite, one 27 inch section of mostly carbon combined with polyethelene, and two 36 inch sections of polyethelene. Most of the polyethelene used as absorber was doped with boron in order to enhance its neutron absorbing properties. A diagram of the beam dump and absorber wall is shown in Fig. 4.

Filling most of the SM12 aperture after the absorber wall was another helium bag.

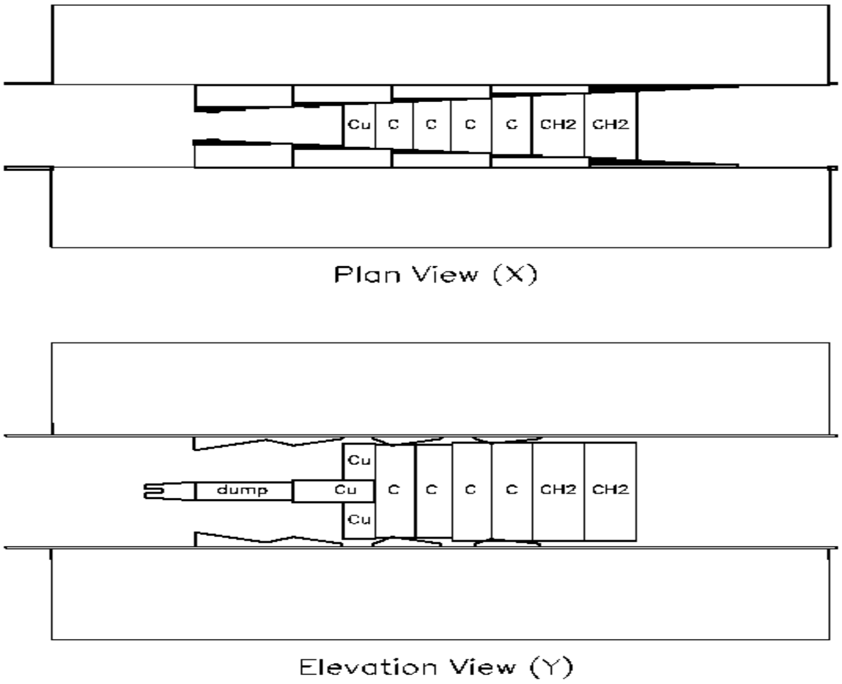

FIG. 4. The SM12 acceptance defining magnet with the absorber wall shown. The magnet coils and iron return yoke are only partially shown. The beam dump is also not shown in the plan view.

The SM3 dipole magnet was between detector stations 1 and 2. This magnet had a 6 foot high by 5 foot wide aperture that was filled with a helium bag, and caused a transverse momentum deflection of 0.91 GeV/c in the tracks of charged particles traveling through it. The SM3 magnet was used together with tracking information from the detector stations to measure the momentum of the muons which were focused into the detection region of the spectrometer by the SM0 and SM12 magnets.

3. *Detector stations*

Directly after the SM12 magnet was the first detector station. The first three detector stations had similar compositions; they all had three drift chambers, and one or two planes of scintillator detectors. Each of the drift chambers had two planes of sense wires, with the two planes offset from each other by half a drift cell. One drift chamber at each station held sense wires that were parallel to the x axis. Since these wires measured the y coordinate of charged particles passing through the chamber, these sense wire planes were called the Y and Y' drift chamber planes. The other two chambers at each station contained wires that were at an angle with respect to the x-z plane. The wires which were at $\approx +14^\circ$ ($\arctan\theta = 0.25$) with respect to the x-z plane were called the U and U' drift chamber planes, and the wires that were at $\approx -14^\circ$ were called the V and V' drift chamber planes. In station four, instead of drift chambers, proportional tube detectors were used to make medium resolution position measurements of the muons. There were three planes of proportional tubes: PT-Y1, PT-X, and PT-Y2. Details of the physical construction of the drift chambers and proportional tubes are shown in Table I; also shown are the voltages at which the detectors were operated.

In detector stations 1, 3, and 4 there were two scintillator hodoscopes which gave a coarse measurement of the y and x positions of particles. At station 2, there were only scintillators to measure the y position of the particles. Each hodoscope was made up of thin, rectangular, scintillator detector "paddles" attached to photomultiplier tubes via light guides. The number of scintillator detectors at each station is listed in Table II. A shorthand notation was used in referring to the scintillator detector planes. The notation "Y1 hodoscope" indicates the station one scintillator plane which measures the y position of a particle. The right or left half planes of

TABLE I. Information on wire chamber detectors. The notation Y2' refers to the station 2 Y' detector. Both the drift cell and aperture sizes are in inches.

detector	number of wires	drift cell size	aperture(X×Y)	operating voltage
Y1	160	0.25	48×40	+1700
Y1'	160	0.25	48×40	+1700
U1	200	0.25	48×40	+1700
U1'	200	0.25	48×40	+1700
V1	200	0.25	48×40	+1700
V1'	200	0.25	48×40	+1700
Y2	128	0.40	66×51.2	-2000
Y2'	128	0.40	66×51.2	-2000
U2	160	0.388	66×51.2	-1950
U2'	160	0.388	66×51.2	-1975
V2	160	0.388	66×51.2	-2000
V2'	160	0.388	66×51.2	-2000
Y3	112	0.82	106×91.8	-2200
Y3'	112	0.82	106×91.8	-2200
U3	144	0.796	106×95.5	-2200
U3'	144	0.796	106×95.5	-2200
V3	144	0.796	106×95.5	-2200
V3'	144	0.796	106×95.5	-2150
PT-Y1	120	1.00	117×120	+2500
PT-X	135	1.00	135.4×121.5	+2500
PT-Y2	143	1.00	141.5×143	+2500

TABLE II. The total numbers of both X and Y scintillators in each detector station.

	number of X counters	number of Y counters
station 1	24	32
station 2	——	32
station 3	24	26
station 4	32	28

scintillators are also often referred to by a similar convention. As an example, the "X3L hodoscope" counters are in the left hand half of the station three X scintillator plane. The Y scintillator planes had a small gap (less than an inch) at x=0, splitting the planes into right and left halves. The X scintillator planes had a similar gap at y=0.

Between detector stations 2 and 3 there was a ring imaging Cherenkov (RICH) detector. This detector was not used to take data for E866, and during the experiment the RICH detector was filled with helium. After station three, there was an electromagnetic calorimeter followed by a hadronic calorimeter, neither of which were activated for E866. They functioned as extra shielding to absorb any hadrons that might have survived past the absorber wall in SM12. There was an absorber wall between the calorimeters and the Y4 hodoscope and PT-Y1 detectors at the front of station 4. Two more absorber walls were in the middle of station 4, between the three proportional tube planes.

The gas used in the drift chambers and proportional tubes was a 50% argon, 50% ethane mixture with a small amount of ethanol, which was added by bubbling the gas mixture through ethanol that was kept at a constant 25° F. The ethanol was used in order to prevent electrostatic deposits from building up on the field and sense wires in the chambers.

B. Detector electronics, trigger, and data acquisition systems

1. *Wire chamber electronics*

In the first three stations pre-amplifiers were attached directly to the drift chamber wires to amplify the electronic signals detected by the sense wires in the chamber. The amplified signals traveled through short cables to discriminators, which compared the signal peak height to a constant threshold voltage. Signals with a peak voltage above threshold voltage were shaped and sent through long cables to time to digital converters (TDCs). These were single hit TDCs, so they were only capable of recording the first hit present on a wire during an event. In station four, signals from the sense wires of the proportional tubes went to combined pre-amplifier/discriminator cards attached directly to the detector planes. Proportional tube signals which were above threshold were sent through cables to coincidence registers (CRs).

2. *Scintillator electronics and trigger system*

A new trigger system was designed for E866 [14] that relied only on scintillator information in order to determine if an event might be worth recording to tape. The trigger system was made up of CAMAC and NIM logic modules, several of which were custom made to be used with this spectrometer. A basic block diagram of most of the trigger system is shown in Fig. 5. The trigger operated as a parallel pipeline, which was synchronized to the RF clock at several points.

Light from the scintillators was amplified by photomultiplier tubes; their outputs were transmitted down long cables, through variable delay modules, into LeCroy 4416 discriminator CAMAC modules. As mentioned previously, there were seven planes

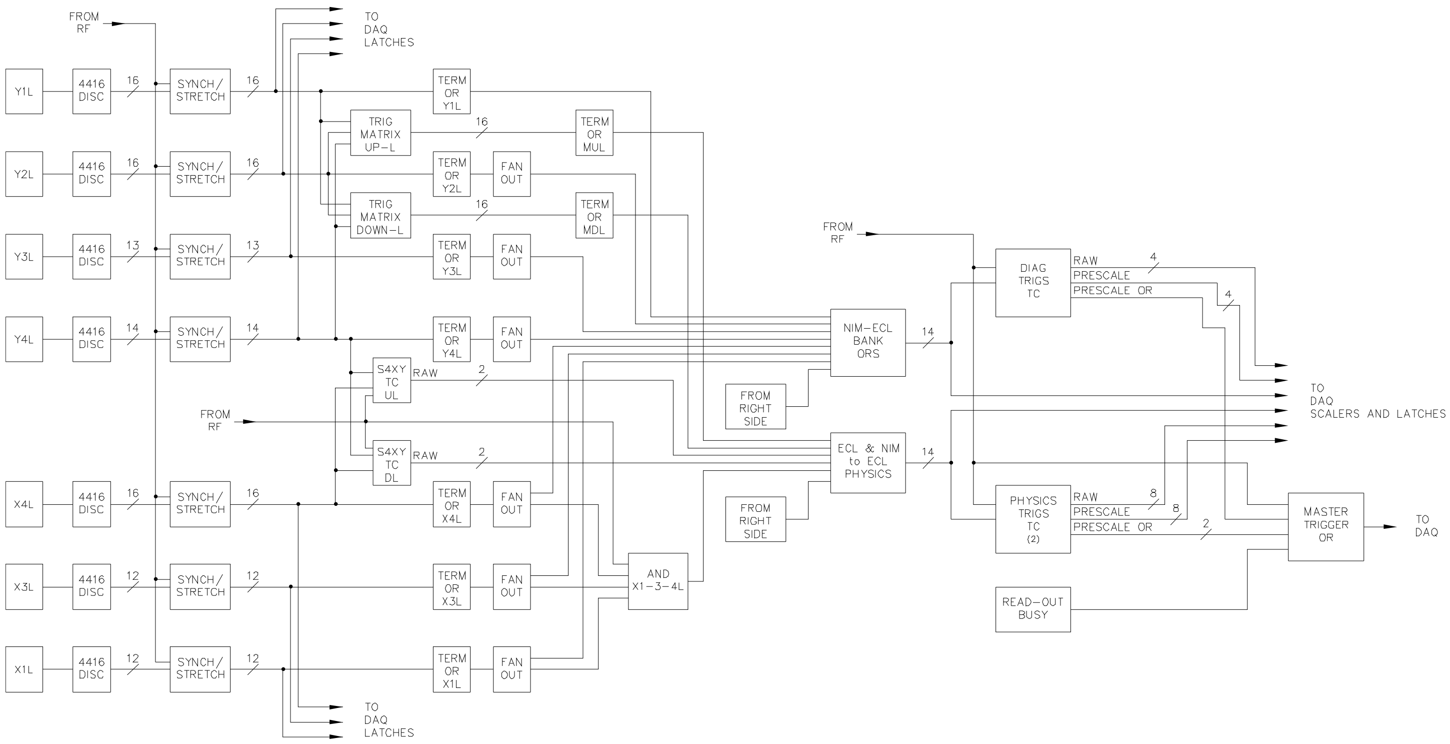

FIG. 5. A block diagram of the E866 trigger system. Note only the inputs and associated electronics for the left half of the spectrometer are shown.

of scintillator detectors. In the trigger system, each of these planes was split into right (negative x) and left (positive x) halves. All of the photomultiplier tubes from each half plane sent their signals to a single 4416 discriminator. The outputs of each LeCroy discriminator went into Stretcher/Synchronizer [15] modules which shaped the signals from the discriminator to a fixed width of 15 ns, and also synchronized the output signals with the RF clock. Each stretcher module produced two copies of these shaped and synchronized signals. One set of signals went to CRs to be latched so that the data acquisition system (DAQ) could read them out to tape. The other set of signals went to Terminator/OR modules, which produced an output of the logical OR of all of the signals from the stretcher module.

The signals from the Y1, Y2, and Y4 scintillators were also presented to Trigger Matrix module [16] inputs before the signals were terminated in the Terminator/OR modules. The Trigger Matrix modules were the main components of the trigger which attempted to identify tracks of muons originating from the target. During normal data taking, the majority of the dimuons in the spectrometer came from the decay of J/ψ particles produced in the beam dump. Monte Carlo studies were used to identify which parts of the acceptance were illuminated by these muons from the dump. It was found that muons from J/ψ decays in the dump and muons from the target could be distinguished from each other much of the time by looking at the pattern of Y1, Y2, and Y4 scintillators hit by the muons. Three dimensional matrices were made of the Y1, Y2, and Y4 hits that indicated possible tracks of muons from the target.

There were four sets of Trigger Matrix modules called MUL, MUR, MDL, and MDR; the notation MUL stands for Matrix Up Left, and similarly MDR stands for Matrix Down Right. The up designation refers to Trigger Matrix modules which detected muons that went above the center of the beam dump and were deflected down by the SM12 magnetic field. Similarly the down designation refers to Trigger

Matrix modules which detected muons that went below the center of the beam dump and were deflected up by the SM12 magnetic field.

A single matrix, such as MUL, was implemented by four Trigger Matrix CAMAC modules, each of which had inputs from twelve Y4, eight Y2, and four Y1 scintillators. The Y4 and Y2 inputs to a Matrix module formed the address inputs to a set of six 256$\times$4 bit ECL SRAM chips. The first output bits from all six SRAMs were ORed together to form a single bit. The second, third, and fourth SRAM outputs were similarly ORed together. If there was a coincidence between one of these four bits from the SRAMs and the corresponding Y1 input to the Matrix module, then the module passed on a signal indicating that a possible muon track had been found.

Another method to identify muons produced from J/ψ decays in the beam dump was the x-y position of both muons at station 4. From Monte Carlo studies it was found that the two muons from a J/ψ decay predominately land in two small areas of station 4. This knowledge could be used to veto events in which muons were detected by the X4 and Y4 scintillators in both of these two areas of station 4. This was done by sending X4 and Y4 scintillator signals to four Track Correlator modules, which will be described in more detail later, before the signals ended at the Terminator/OR modules. Each of these Track Correlator modules had as inputs the X4 and Y4 scintillator signals from a quadrant of station 4. If an X-Y coinicidence was detected in the "veto area", the Track Correlator output a signal indicating that a hit was found in the "veto area" of that quadrant. These four Track Correlator modules are also referred to as S4XY modules.

In a limited fashion, the X scintillators were also used in the trigger system to identify dimuon events. A signal was produced with simple NIM logic modules, called X134L, when there was a three fold coincidence between the X1L, X3L, and X4L Terminator/OR outputs. A similar signal, X134R, was produced from the right hand scintillator signals.

Track Correlator (TC) modules were used to select specific patterns of Trigger Matrix, Terminator/OR, and S4XY outputs to trigger on an event. A block diagram of the internal data flow of a Track Correlator is shown in Fig. 6. The Track Correlator modules had 16 data inputs which were fed into a 10 ns 64K$\times$4 bit SRAM chip that was the heart of the module. These SRAMs could be programed with four independent trigger conditions. Each trigger condition was a set of any number of input bit patterns. The four SRAM trigger outputs were synchronized with the RF, and also could be prescaled by on-board 12-bit programmable prescalers. As shown in Fig. 6, both the prescaled and unprescaled (raw) signals from all four triggers were output by the module, as well as the logical OR of the four prescaled trigger signals.

There were three main Track Correlators which were able to trigger on an event to start the DAQ recording that event. Two of these modules were called Physics TC A and Physics TC B; the third module was called the Diagnostic TC. The two physics TC modules were used to trigger on the physics events that the experiment was interested in. The inputs to the physics TCs included the Trigger Matrix and the S4XY outputs, as well as the X134L and X134R signals. The Diagnostic TC had as inputs all fourteen Terminator/OR outputs. As the name suggests, the Diagnostic TC was used to diagnose problems with the trigger system. It was also used to "exercise" and monitor the trigger and DAQ systems during long periods with no beam by triggering on cosmic rays, and it was used as the main trigger for scintillator efficiency measurements.

After a Track Correlator had decided to trigger on an event, its decision was sent to the Master Trigger OR, which then determined whether or not the event was to be recorded to tape. The Master Trigger OR synchronized both trigger signals and changes in the busy status of the DAQ with the RF clock. This ensured that

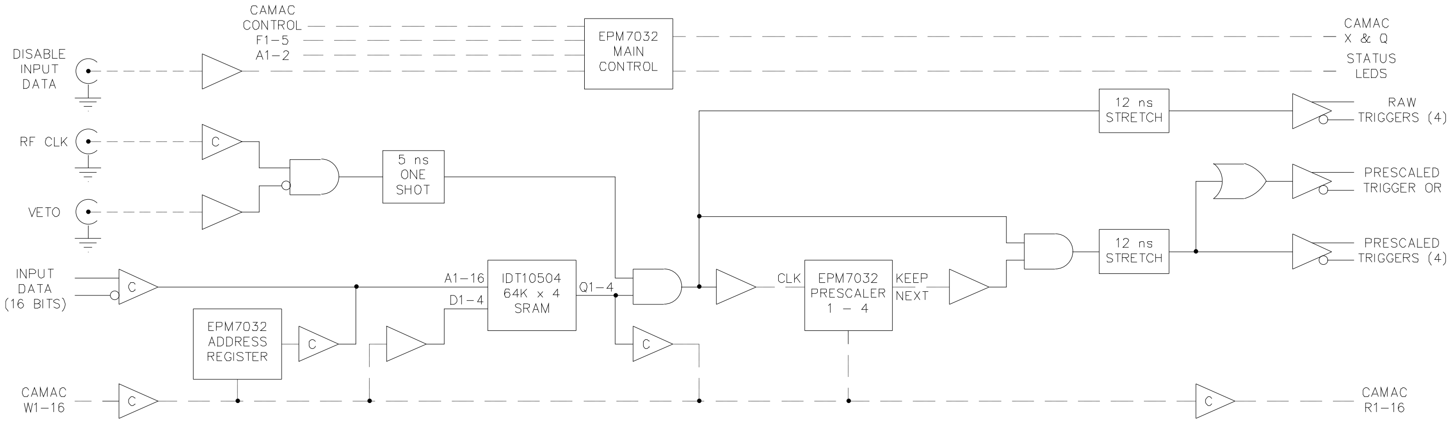

FIG. 6. A diagram showing the data flow in a Track Correlator module. To simplify the diagram, the control lines connecting the main control circuit to the prescalers, the SRAM, and the various buffers and level translators are not shown. The components labeled with a C are enabled and disabled by the main control circuit.

the DAQ busy status was in a well defined state when a trigger was received by the Master Trigger OR. While the DAQ recorded an event to tape, the DAQ busy was enabled. Only when the DAQ busy was disabled was the Master Trigger OR able to send trigger signals to various parts of the DAQ to start them recording an event.

3. *Data acquisition system*

The data acquisition system was responsible for compiling, formatting, and recording the raw data on magnetic tape for storage. It was a mixture of Nevis Transport [17] electronics, VME modules, and CAMAC modules. The Nevis Transport system was also referred to as the readout system since it was responsible for "reading out" the data from the detectors and trigger so the remainder of the DAQ could record the data to tape. The readout system included TDCs which measured the drift times of wire chamber hits, CRs which latched both the proportional tube and scintillator detector hits, and the trigger bit latch system which stored trigger and target position information about events. The trigger information that was recorded included the outputs from the Terminator/ORs, Trigger Matrices, and all of the Track Correlators, including the S4XY modules. When the DAQ received a trigger signal, the readout system then collected the event data from all of the modules mentioned above, and then the DAQ stored the data in large memory buffers. These memory buffers allowed the DAQ to decouple the rate at which events were being triggered from the rate at which data were being written to tape.

In addition to the event data the DAQ also recorded information about each spill and each run. The data collected on a spill by spill basis included target positions and pressures; beam intensity and position; currents of the three magnets; and the scaler sums of the Terminator/OR outputs, Trigger Matrix outputs, and Track Correlator outputs. The configuration of the spectrometer and trigger was recorded at the beginning of each run.

Data acquisition software, running on a VME single board computer, controlled the flow of data from the readout system, through the memory buffers, to an 8mm magnetic data storage tape. This software was also responsible for loading the trigger at the beginning of each run, as well as other beginning and end of run tasks. Whenever the CPU was booted or reset, the entire set of DAQ software was loaded into the single board computer over the network from the disk of a Silicon Graphics workstation. The Silicon Graphics workstation also received information over the network from the Fermilab EPICURE system which collected data from the parts of the beamline not under the direct control of E866. It is through the EPICURE system that the information from ME6SWIC and the SM0 magnet voltage, for example, was collected. The Silicon Graphics workstation recorded this information in an online database.

CHAPTER III

EXPERIMENTAL PROCEDURES

Preparing the spectrometer to take data required a great deal of effort and hard work by many people, and equally as much work was needed to keep the experiment efficiently recording data. This chapter will go into detail about the preparations required before taking data, procedures used during data taking, and the types of data collected.

A. Initial setup and calibration

1. *Pre-run preparation*

Because of the changes made to the spectrometer as well as the amount of time since it was last used, a great deal of preparation, testing, and calibration work was needed before E866 could take data. A new set of larger station 1 drift chambers and scintillators was designed, constructed, and installed in order to increase the acceptance of the spectrometer. All detector electronics, such as pre-amplifiers and discriminators, were tested and repaired if necessary, and the long cables needed to connect the detectors to the trigger and DAQ were also tested, repaired if necessary, and reinstalled. A new trigger system was designed, the implementation of which required the design and fabrication several new electronics modules. The DAQ underwent significant enhancements, the most important of which was with respect to the extensive software used to control the flow of data to tape. Much of the gas system used for the wire chambers was replaced, and the gas safety and monitoring systems were updated.

In order to accurately analyze the data from the spectrometer, precise knowledge of the magnetic fields throughout all three magnets was required. The fields of all three magnets had been determined by field mapping for previous experiments. However, unlike previous experiments, SM0 was positioned very close to SM12 for E866, causing their fields to overlap. Because of this the magnetic fields were re-mapped in both SM0 and the front quarter of SM12. The mapping of the magnets was done by measuring the magnetic fields on a three dimensional grid inside the magnets with a 2 inch spacing between grid points. The fields in SM12 were mapped at magnet currents of 2040 and 2800 amperes before SM0 was installed. When SM0 was present it was run with currents of +2100, 0, and -2100 amperes. For each of the SM0 current settings, both magnets were mapped with SM12 currents of 2040 and 2800 amperes. The magnets were not mapped with an SM12 current of 4000 amperes because that magnet setting was not expected to be used. However, it was used, and a magnet simulation program was used to create a 4000 ampere field for SM12 by extrapolating from the field measured at 2800 amperes, and combining the result with a previous 4000 ampere field map.

2. *Detector testing and calibration*

Before E866 received beam on target, beam was sent periodically to the Meson Center beam dump during initial accelerator tuning. The Meson Center beam dump was some 1400 feet in front of the E866 targets. The Tevatron beam hitting the Meson Center dump produced a very low rate of single muons that would pass through the E866 spectrometer if all three of the magnets were off. By using a very simple trigger loaded in the Diagnostic TC, data on these single muons were recorded to tape. A simple analysis of this data was very helpful in measuring the relative alignment of the hodoscopes and the sense wires in the drift chambers, and was also helpful in setting the correct timing for the TDC gates.

After the experiment began receiving beam on target, but before the start of data taking, the timing and efficiencies of the detectors were studied using muons produced at the target. High voltages used for the wire chambers and photomultiplier tubes were adjusted to maximize the efficiency of the detectors while keeping the noise rates low. The timing of each scintillator signal was adjusted with a variable delay box so that it arrived at the Stretcher/Synchronizer in time with all of the other scintillator signals and in time with the Tevatron RF clock.

The trigger system was tested by setting bit pattern masks in the LeCroy 4416 discriminators, and causing them to fire test pulses with that bit pattern synchronous with the RF. In this way, any pattern of scintillator signals could be artifically produced. Both the inputs and the outputs of the Diagnostic and two Physics TCs were latched in LeCroy 4448 CAMAC coincidence registers for each test pulse. A software simulation of the trigger was used to analyze the results found by the trigger system for each test pulse input into it to determine if the trigger had worked correctly. The DAQ was tested in a similar way, by supplying the system with fake event information and analyzing what was recorded to tape.

B. Data taking procedures

1. *Monitoring the experiment*

The majority of the work done while the experiment was in progress dealt with monitoring the many systems and detectors used in data taking. At least one person was on shift at all times while the experiment was running. The job of the person on shift was to keep the experiment operating at peak efficiency at all times. Shift checks were done twice a day to check on the gas and target systems, and to do a general inspection of the experimental apparatus. While data was being collected, the intensity, size, position, and consistency of the beam was continually monitored.

If any of these beam qualities varied outside acceptable limits, the person on shift was responsible for calling an accelerator operator to correct the problem.

Several quantities were monitored by the use of scalar modules. These modules integrated the chosen quantity over the course of a spill and continually displayed their results for the person on shift to see. The scalars were used to monitor such quantities as beam intensity, live time, and duty factor. Several trigger and scintillator quantities were also monitored with the scalars; these included the raw number of hits from each TC trigger, each trigger matrix, and each scintillator half-plane.

A large database was used to store the scalar information from each spill. Also stored in the database were several quantities which were not recorded by the scalars. These included magnet voltages for SM0, SM12, and SM3, and beam size and position measurements. The database was constructed so that the stored information could be easily retrieved and analyzed in order to study systematic effects.

A fraction of the events which the DAQ recorded to tape were also transmitted over the network to the Silicon Graphics workstation. These events were sent through an on-line analysis program in order to monitor, among other things, the hit distributions in the wire chambers, scintillator planes, and proportional tubes. Even though this detector information was a small sample of events biased by the trigger, it still was able to indicate large inefficiencies in the detectors caused by malfunctions. Because this event analysis was "on-line" (meaning that it was directly connected to the DAQ), raw event and spill information could be examined as soon as it was recorded by the DAQ.

2. *The initial analysis*

The experiment was monitored in a more complete manner by a full off-line analysis of the data soon after it was recorded. After $\approx$1 Gbyte of data were recorded on a tape, the data taking was stopped, and the tape was replaced with a new one. The data on the full tape was then read out onto a disk of a Hewlett-Packard workstation. Unlike the on-line analysis, the off-line analysis was able to do a full event reconstruction of all the events recorded by the DAQ. This initial analysis, done on Hewlett-Packard workstations, was used to produce only preliminary results, since many adjustments of analysis parameters were still needed to optimize the resolution and reconstruction efficiency.

There were three main reasons for the initial analysis. As mentioned above, this analysis provided a complete way to monitor the experiment. The initial analysis included some simple trigger checking routines which detected malfunctions in the trigger during the data taking. The detection efficiency for each wire chamber was also monitored with this analysis. When all of the chambers were working correctly, the detection efficiency for each chamber was above 96%, and the average efficiency of all the chambers was over 98%. A basic goal of the experiment was to detect and record "good" dimuon events that could be reconstructed by the off-line analysis. The initial analysis allowed the number of "good" events recorded per unit beam intensity to be monitored. Any significant deviation in the rate of "good" events signaled that something was not working correctly. The initial analysis also allowed the experiment to examine the first basic physics results from the data. The dimuon mass spectrum resulting from this initial analysis showed peaks for the J/ψ and Υ resonances with close to the expected masses and resolution. Early in the experiment this provided an important verification that the experiment was working correctly.

In addition to monitoring the experiment and examining the first physics results, the initial analysis was used to determine what adjustments were needed in the analysis code before the complete analysis was performed. Among other things it was found that adjustments were needed in the SM12 magnetic field map and the energy loss and multiple scattering corrections to optimize the spectrometer resolution.

Because of the trigger bias in the events recorded, the initial analysis of the data was not able to accurately measure the detection efficiency of all the scintillators. Several times during the experiment, small amounts of data were taken with a special single muon trigger loaded in the Diagnostic TC. This data was analyzed with a modified analysis program to extract the detection efficiency for each scintillator. If the detection efficiency for a scintillator was found to be below 95%, the high voltage for that detector was increased if possible. In order to prevent damage to the photomultiplier tubes, their high voltage was not allowed to be set over 2100 volts. When working correctly, typically the average detection efficiency for a plane of scintillators was above 98%.

C. Data sets

As mentioned previously, the purpose of the SM0 and SM12 magnets was to collect and focus as many muons as possible into the detection region of the spectrometer. By changing the magnetic fields in SM0 and SM12, the acceptance of the spectrometer could be shifted to enhance the detection probability for events with different dimuon masses. The experiment took data at three mass settings: low, intermediate, and high. Each mass setting was further broken down into data sets, which correspond to different experimental conditions. Shown in Table III are the mass settings, data sets, and magnet settings which were used to collect Drell-Yan data from the liquid targets. As an example, data set 2 was ended and data set 3 started when the Tevatron beam tune was changed and the beam quality (as measured by the duty factor) improved dramatically.

There was a slight difference in the spectrometer's acceptance for muons depend-

TABLE III. Magnet currents for the different data sets and mass settings are shown. All magnet currents are in amperes. The SM3 magnet was always operated at 4230 amperes with the same polarity as SM12.

mass setting	data sets	SM0 current	SM12 current
intermediate mass	1,2,3,9	0	2800
	4	0	-2800
low mass	5	-2100	2800
	10	2100	-2800
high mass	7,8	0	4000
	11	0	-4000

ing on whether they traveled above or below the center of the beam dump. This was because of a slight angle to the beam when it hit the target and because SM12 and the beam dump have sunk slightly ($\approx$ 1/2 inch) over the years. To study this effect, some data were taken with the magnet polarities reversed. The magnet current polarities shown in Table III correspond to the direction in y in which the magnetic fields bend postitively charged particles. So, in data set 7 the magnetic field in SM12 bent protons in the positive y direction (up). The SM3 magnet was always run at a current of 4230A with the same polarity as SM12.

There were two different purities of deuterium available for use in the deuterium target. Because it cost $\approx$ \$2000 for the target to be filled once with the "good" deuterium, this higher quality gas was used only when it was reasonably certain that the targets would not be emptied for a long period of time. At the beginning of the experiment, in September of 1996, the collaboration was unsure of the cryogenic targets, and so chose start with the "bad" deuterium. After several problems with the cryogenic system were discovered and fixed, the target was filled with the "good" deuterium between data sets 1 and 2. During the Christmas shutdown at the end of 1996 the targets were emptied. When the experiment started up again in January target problems were expected, so the "bad" deuterium was used. However, problems with the target cryogenics did not occur, and there were no opportunities to switch to the "good" deuterium without losing two days of beam time. So all data sets after data set 7 were taken with the "bad" deuterium. The two different purities of target deuterium, and their effects on the data analysis are discussed in further detail in chapter IV.

D. Trigger configurations

For each mass setting, trigger matrices were calculated using a Monte Carlo simulation of the spectrometer. These matrices were basically simple "lists" of Y1-Y2-Y4 scintillator triple coincidences, called cells, which would indicate a possible muon originating from the target. These "lists" were then loaded from a UNIX workstation, via the DAQ VME control processor, into the SRAMs of the Trigger Matrix modules. One of the basic trigger philosophies for E866 was to trigger on as many potentially "good" events as possible, but at the same time maintaining an experimental dead time of less than 2%. A larger dead time could lead to larger rate dependent effects, which in turn could produce a larger systematic uncertainty. Both dead time and rate dependence will be discussed in more detail in the next chapter. Since the goal of E866 was to perform a high precision measurement, the trigger and beam intensity were adjusted, by two different techniques, so that the event rate did not cause a large experimental dead time.

Whenever a new trigger configuration was implemented, a small amount of data was taken with the new trigger matrix. This data was then analyzed to see how many "counts" were detected for each matrix cell. Usually several matrix cells had over an order of magnitude more counts than the average number of counts in all the other cells. The majority of the muons detected in these "hot" cells originated from the beam dump, but some of the muons were still from "good" events which occurred in the target. If the dead time was too high, a few of these hot cells were deleted from the trigger matrix, and more data were taken and if necessary more cells were removed from the matrix. This continued until either the dead time was reasonable, or there were not any hot cells left to remove.

As mentioned in the previous chapter, another part of the trigger was the S4XY veto. The veto areas in station four were two small triangular regions at the center of the top and bottom of the detector station. If a coincidence between X and Y scintillators occurred in both veto areas, then the event could be vetoed at the trigger stage. In addition to removing cells from the trigger matrix, the trigger rate could be adjusted by changing the size of the S4XY veto regions.

Four different trigger conditions (refered to as "triggers" below) were able to be loaded into each of the Physics TC modules. Two types of triggers were used in these modules. "Physics" triggers were used to collect the types of events the experiment was most interested in, namely dimuon events. Triggers of this type were always prescaled by 1 in the TC to keep every event. The other type of trigger used was the "study" trigger. These were used to collect data in order to study systematic effects of the experiment such as detector efficiency and random coincidences. The study triggers were prescaled in the TC, some by factors as large as 4000. The TC prescalers for these triggers were set so that these triggers contributed a small amount to the overall trigger rate of the experiment.

In order to load a trigger into a TC, an easily understood "human readable" configuration file was created on a UNIX workstation. This file was then transformed into a “computer readable” bit pattern file which the DAQ processor read over the network. The DAQ then loaded this bit pattern into the SRAM of the TC module by using basic CAMAC commands. Below is an example of a “human readable” trigger for the Diagnostic TC.

DIAG1 = 1 OF

((X1L + X1R) * (Y1L + Y1R)) + ((X1L + X1R) * (Y2L + Y2R)) +

((Y1L + Y1R) * (Y2L + Y2R));

The * symbol represents a logical AND, the + represents a logical OR, and the “DIAG1 = 1” phrase means the first Diagnostic TC trigger was prescaled by 1. This particular trigger would select all events that include hits in at least two of the three detector planes X1, Y1, and Y2.

There were three physics triggers used for the high mass data setting. One trigger required a MUL·MDR or a MDL·MUR coincidence, another trigger required a MUL·MDL coincidence, and the third trigger required a MUR·MDR coincidence. These three opposite sign dimuon triggers formed the basis of the physics triggers for all three mass settings. The three study triggers used for the high mass setting were: a MUL·MUR or a MDL·MDR coincidence, a X134L·X134R coincidence, and any matrix. The first of these triggers was used to collect events with two muons with the same sign. The “any matrix” trigger was a highly prescaled trigger used to collect single muon events. Both of these triggers were used to study the background events caused by two random single muons in coincidence. Since the triggers which only use matrix outputs depend on Y scintillator information only, the second study trigger was used to examine the efficiency of the Y scintillators.

The triggers used in the low mass setting were very similar to those in the high mass setting. The S4XY outputs were included in the MUL·MDL and MUR·MDR triggers in order to require two x-y coincidences in the station 4 scintillators. Whenever the S4XY outputs were used in a physics trigger, a study trigger was created to record a sample of the events rejected due to the S4XY information.

The S4XY outputs were also used in the triggers for the intermediate mass setting. All three of the opposite sign diumon physics triggers required that at least one muon pass through station 4 outside the S4XY veto region. The intermediate mass setting also had the same study triggers as the high mass setting in addition to a trigger that sampled the events vetoed by the S4XY outputs.

The final way of decreasing the event rate and dead time was to decrease the beam intensity. The beam intensity requested by the experiment was limited by either the particle detection rate in station 1 or by the maximum intensity allowed for the experiment. For the low mass setting, the requested beam intensity was usually 5×10^{11} protons per spill. At higher beam intensities, the number of particles going through station 1 per RF bucket became so large that the efficiency of the wire chambers significantly decreased. For the high and most of the intermediate mass settings, the requested beam intensity was 2×10^{12} protons per spill. This was the maximum beam intensity allowed due concerns about radiation safety and beam induced heating of the cryogenic targets.

CHAPTER IV

THE CALCULATION OF THE RATIO OF CROSS SECTIONS

From the initial analysis of the data, it was learned that it would be necessary to correct for several systematic effects such as events due to random coincidences and rate dependent efficiencies. It was also found that these corrections were the easiest to implement for the high mass data set. Because of this, a complete analysis was done on the high mass data first in order to extract a physics result and to develop and better understand the methods to measure and correct for these systematic effects. The remainder of this dissertation will deal with the analysis and results exclusively from the high mass data sets.

The calculation of the ratio of cross sections, $\sigma^{pd}/2\sigma^{pp}$, required two kinds of information. First was the number of Drell-Yan events as a function of x from each target. To get this, raw event data were analyzed, filtered, and corrected for random coincidences and backgrounds. Second, the ratio calculations required several relative target normalization factors such as target densities, rate dependences, and the amount of beam on each target. These analysis issues are discussed in detail in this chapter.

A. Event analysis

Three separate analysis passes were made on the high mass data sets. The first two passes were devoted to muon tracking and event reconstruction. They used conservative criteria to accept events in order to be certain that as many good events were reconstructed as possible. These two passes used the same basic analysis code, which will be described below. The first pass was done on the Fermilab parallel computing farms, and was mainly responsible for weeding out "bad" events. Of the events that were recorded to tape during the experiment, less than 0.5% of them were able to be reconstructed into candidate dimuon events by the first pass analysis. The second pass analysis, done on Hewlett-Packard workstations, was mainly devoted to improving the resolution of the kinematic variables. This was partly accomplished through improvements in magnetic field maps, and the energy loss and multiple scattering calculations. In order to fine tune these improvements in the analysis code, the full second pass analysis was run several times. Over 80% of the events kept by the first pass analysis were also kept by the second pass analysis as dimuon events. The third analysis pass selected the final events used in the calculation of the ratio of cross sections. This analysis was designed to minimize background contributions and systematic uncertainties for this calculation.

1. *Muon tracking*

The analysis code used for E866 was originally written for E605 [13]. Since then it has been greatly modified, however the basic method used for analyzing events has not changed. Initialization and setup routines were run at both the start of the program, and at the beginning of each run found in the data. This ensured all data from a given run were analyzed with the correct run conditions, such as magnet surveys and trigger configurations. The data was originally written to tape in a specific binary format unique to our readout and DAQ systems. So, following initialization and setup, the analysis program had to translate or "unpack" the data into arrays usable by fortran.

The reconstruction of an event began by examining the patterns of "hit" wires in the drift chambers of stations one, two, and three. The term "hit" refers to a particle passing through a drift cell or scintillator, and being detected by the sense wire or photomultiplier respectively. There are two types of hit patterns that the analysis code looked for, triplets and doublets. A triplet is when there is a hit in a station's drift chambers in at least one Y or Y' wire, one U or U' wire, and one V or V' wire that all intersect at one drift cell. Also required for a triplet is at least one associated hit. An associated hit is when a particle hits both the primed and un-primed wires of a chamber. For example if a particle hits both a Y and a Y' wire, then the Y' wire that was hit is associated with the hit Y wire. A doublet is when only two of the three "views" (Y, U, and V) are present at an intersection, but with two associated hits. For both triplets and doublets, the drift times of the various hits, especially the associated hits, must be correlated with each other in order to show that all of the hits were caused by a single particle.

For each triplet or doublet found in station three, the analysis code scanned through all of the triplets and doublets found in station two, and made a track segment by connecting the hits in station three with the hits in station two. Each track segment was checked with respect to several criteria to ensure that it could have been the track of a muon originating from the target. As an example, if the track segment was extended to the bend plane in SM3 and to the back of station four, the track had to stay inside the physical acceptance of the spectrometer, otherwise the track segment was discarded.

Once the analysis program had found all the valid track segments, each segment was projected back to station one, where a "window" in y was defined taking into account the magnetic field in SM3. If a doublet or triplet was found in the "window" at the correct x position, then the code was able to calculate both the sign and the momentum of the muon from the bend in the track caused by the SM3 magnetic field. Again checks were made to discard any tracks that were not consistent with a muon produced at the target. The track was also projected to station four and was discarded if signals were not present, in the correct locations, from at least three of the five detector planes in that station (two scintillator, and three proportional tube).

After the sign, position, and four momentum of the muon were known at station one, the analysis program could project the muon's trajectory back through SM12 and SM0 to the target. In the routine PBSWIM, the muon's path through SM12 was calculated, and corrections were applied for energy loss in the absorber wall and the beam dump. Also, this routine corrected for any scattering that occurred as the muon passed through the absorber wall and the beam dump.

In the second pass analysis, the PBSWIM routine worked as follows. Starting at SM3, the muon's track was calculated back to the end of the absorber wall. The beam dump and absorber wall were split into sections, and the muon's track was stepped through SM12 section by section. The path of the muon was calculated by using the SM12 magnetic field maps, the position and momentum the muon had exiting the previous section, and the energy loss suffered by the muon in the current section. This continued, section by section, until the muon's track had been traced to the front of the beam dump. As the muon's trajectory was traced through the area of SM12 containing the beam dump, the length of dump through which the muon traveled was recorded. This length was used in determining the z position of the scattering bend plane for this track.

Due to the extreme thickness of both the absorber wall and beam dump, muons passing through them usually underwent several small angle scatters. This caused a loss of both position and momentum resolution at the target. This loss of resolution was reduced by approximating all of the scattering that the muon experienced in the absorber and dump, and applying it to the muon's track at a single scattering bend plane.

To use the scattering bend plane, the muon's track again starts from SM3, and was traced back through SM12 and SM0 to the z position of the target, taking into account the energy loss in the absorber and the dump as mentioned above. This is referred to as the uniterated track. The uniterated x and y positions of the track at the z position of the target were used to determine a small angular deflection to be applied to the momentum of the muon at the scattering bend plane. Then, starting at the scattering plane, the muon's track was retraced through SM12 and SM0 to the target, and the new iterated x and y positions of the track at the z of the target were used again to adjust the momentum at the scattering plane. This iteration continued until both the x and y positions of the track at the z position of the target were within 0.1" of the center of the target. The PBSWIM routine in the first pass analysis was similar to that used for the second pass analysis except it used a single fixed scattering bend plane for all muons.

2. *Reconstruction of muon pairs*

Once both the energy loss and scattering had been corrected for, the track angles and the total momentum at the target for each muon were passed to the DIMUSE routine. In DIMUSE these quantities were used to calculate the four momentum at the target for each muon. The single muon four momenta were then used to calculate the kinematic quantities for one (or more) dimuon event(s). In the data from the high mass setting, there were very few good events (< 20) that had three or more good tracks from the target. Some of the kinematic quantities calculated for each dimuon event were mass, x_F, x_1, x_2, and transverse momentum (p_T).

After an event had been fully analyzed, the final results, as well as many of the intermediate results such as track positions and angles at various points in the spectrometer, were stored in both an ntuple and histograms. An ntuple is a large two dimensional array, with one dimension being the number of events, and the other dimension containing information on each event in a large number of variables. In addition to the event information, both the ntuple and the histograms also had information about all spills that occurred during data taking, whether or not any "good" events were recorded during that spill. Most of this "spill" information related to various raw detector and trigger rates. Other "spill" quantities included beam intensity, live time, target position, beam duty factor.

The second pass analysis was able to reconstruct over 200,000 dimuon events, of which over 25,000 events were part of the Υ family of resonances. As shown in Fig. 7, these dimuon events ranged in mass from 2.0 GeV/c^2 to 19 GeV/c^2, and the x of the target parton ranged from below 0.01 to above 0.35.

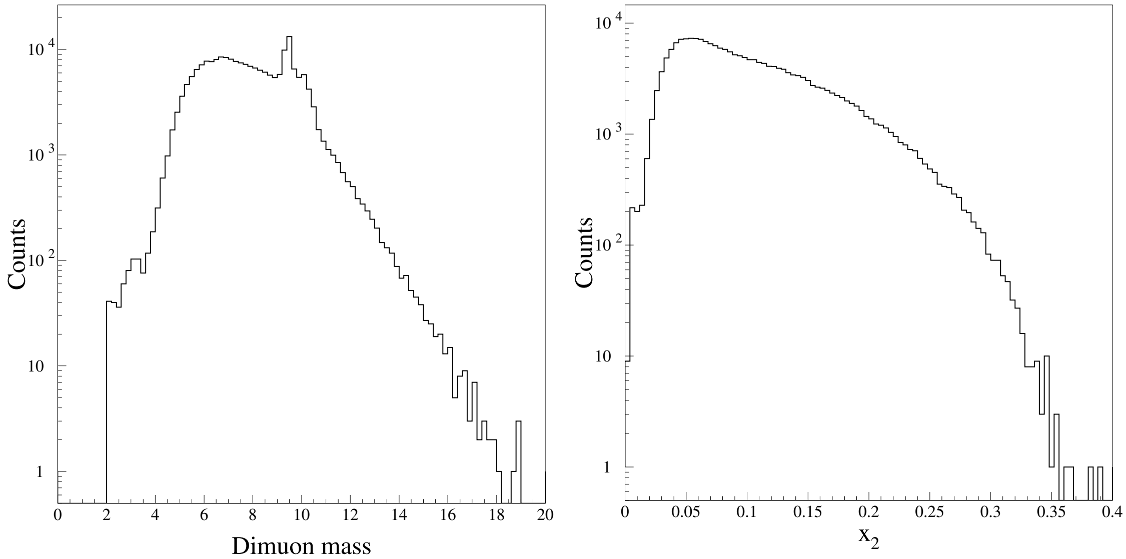

FIG. 7. The mass and x_2 distributions of events reconstructed by the second pass analysis. The dimuon mass is shown in units of Gev/c^2.

3. *Ntuple cuts*

After the second pass analysis the remaining events, stored now in ntuples, were subjected to a final set of "cuts". These cuts were very carefully examined and tuned in order to extract only good "clean" Drell-Yan events. Approximately 68% of the events reconstructed by the second pass analysis also passed all of the ntuple cuts. Events with a dimuon mass between 9.0 and 10.7 GeV/c^2 were cut in order to remove the Υ, Υ', and Υ'' resonances from the data. This cut on dimuon mass was responsible for removing four times as many events from the data sample than all the other ntuple cuts combined. Events with a dimuon mass less than 4.5 GeV/c^2 were also cut. This was to ensure that events from the J/ψ, and ψ' were excluded, and to reduce the number of events due to random muons.

In addition to improving the kinematic resolution, the second pass analysis also calculated which trigger bits the reconstructed muon pair should have fired. If all of the trigger bits that should have fired are not present, then it is not certain if the event that was reconstructed was responsible for firing the trigger. Since the acceptance of the spectrometer is in part defined by the trigger, any Drell-Yan event that did not satisfy the trigger check is, by definition, outside the acceptance. As will be discussed later, it is of crucial importance that the acceptance for events is identical for all three of the targets. To ensure this remains true, events were cut if the reconstructed tracks in the event were not responsible for firing the trigger.

Cuts were made with respect to the total dimuon momentum and the transverse dimuon momentum. Events with a total dimuon momentum greater than 800 GeV/c were cut because of momentum conservation. A cut at 7.0 GeV/c in transverse dimuon momentum was made to remove background "bad" events as seen in the p_T spectra shown in Fig. 8.

Three cuts were made using the uniterated quantities of the event vertex. This was done to reduce the number of Drell-Yan events that originated outside of the target. Events were cut if, at the z position of the target, one of the uniterated tracks had a position in the x y plane more than 2.5 inches from the beam. The apparent z position of the dimuon event vertex before iteration, which was called the "zunin" of

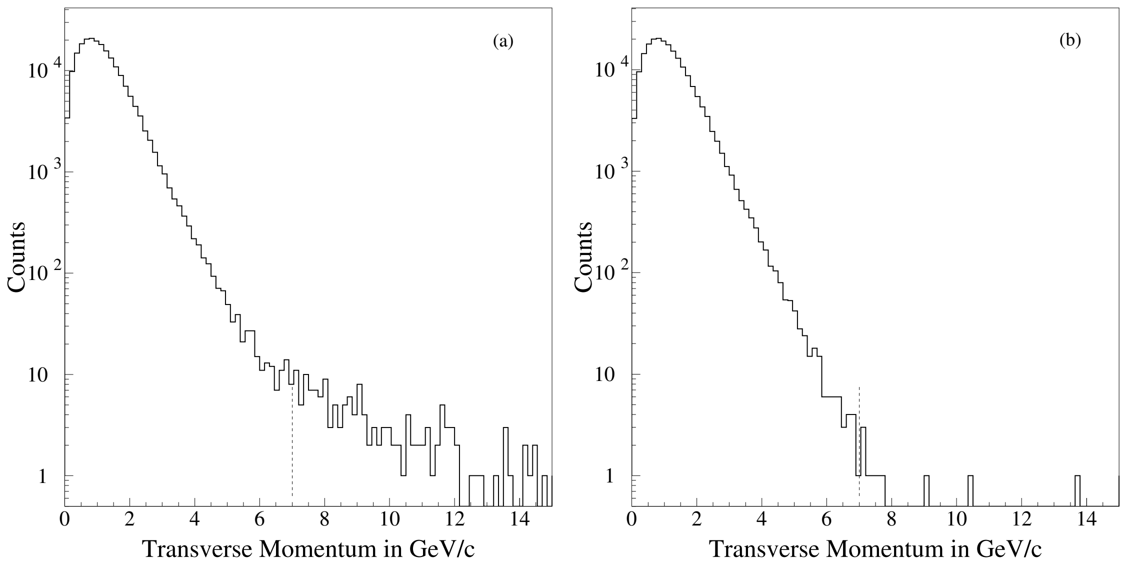

FIG. 8. The p_T spectra of events passing (a) just the total momentum cut and (b) both the total momentum and the trigger cuts. The dashed line shows the value of the ntuple cut made on the p_T of the event.

the event, was used to separate out as many events as possible that originated from the ME6SWIC. Cuts were made 70 inches upstream and 90 inches downstream from the center of the target. Events with an uniterated vertex outside of these cuts were excluded from the data. Figure 9 compares the zunin distributions for the hydrogen and empty targets. The empty target zunin distribution has been renormalized to the same integrated beam intensity as the hydrogen data shown.

Events were also cut based on the angle of the iterated muon tracks at the target with respect to the beam. If each track angle at the target was less than 26 milliradians in the x-z plane projection, the event was kept. At any larger angle, the muon tracks project through the steel of the SM12 pole pieces. Since the magnetic field, energy loss, and scattering in the steel pole pieces were not well known, these events were not considered “clean” events, and were not used. Two more cuts on

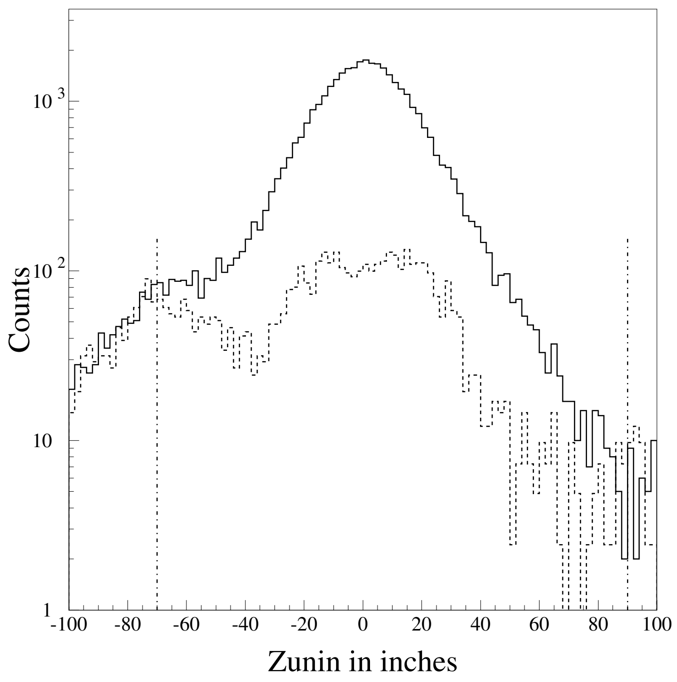

FIG. 9. An example of the zunin distributions for the hydrogen (solid) and empty (dashed) targets. The dashed-dotted lines indicate the cuts used.

the iterated muon tracks at the target ensured that all of the muons with a similar sign travel on the same side of the beam dump. For the majority of the high mass setting data, the polarities of SM12 and SM3 were such that in most accepted events, positively charged muons went under the center of the dump, and negatively charged muons went above.

Four cuts were made – on IC3, duty factor, "event length", and live time – to remove events from spills with low beam intensity or low beam quality. When the intensity of the beam was erratic during a spill, the events recorded from that spill usually came from periods of very high instantaneous beam intensity. High instantaneous beam intensities cause more random coincidences and rate dependent effects, which are discussed later in this chapter. Data from the IC3 beam intensity monitor were used to discard events from spills with little or no beam. Quite often spills with very small amounts of beam occurred due to a Tevatron abort before the end of the spill, and the beam intensity was quite often erratic just before an abort. The duty factor is a measure of the stability of the beam intensity; it is defined as

$$DutyFactor \;=\; \frac{< I(t) >^2}{< I(t)^2 >}, \tag{4.1}$$

where I is the beam intensity in a beam "bucket". In E866 the duty factor was measured with two scintillator detectors, S1REF and S3REF, which were placed outside the spectrometer's acceptance. If the single particles detected by S1REF were uncorrelated with those detected by S3REF, the duty factor is simply

$$DutyFactor \;=\; \frac{[S1REF] \cdot [S3REF]}{[S1REF\ and\ S3REF]} \cdot 10^{-9}, \tag{4.2}$$

where $[S1REF]$ and $[S3REF]$ are the number of hits in each of those detectors per spill, $[S1REF\ and\ S3REF]$ is the number of coincidences per spill between the S1REF and S3REF detectors, and there are $\approx 10^9$ potentially filled buckets per spill. Events from spills with a duty factor less than 25% were cut. A third cut was also used to remove events taken with very high instantaneous beam intensites. A cut was made based on the raw number of scintillators and drift chamber wires that were hit during an event. This cut, also known as a cut on the "event length", is shown in Fig. 10. A cut was also done on experimental live time. If the live time for a spill was not greater than 90%, then the events from that spill were discarded. All four of these cuts were made in an effort to reduce the rate dependence and the number of events due to random coincidences.

Shown in Fig. 11 are the mass and x_2 distributions of the Drell-Yan events from the high mass data sets that were reconstructed by the second pass analysis and survived the ntuple cuts described above.

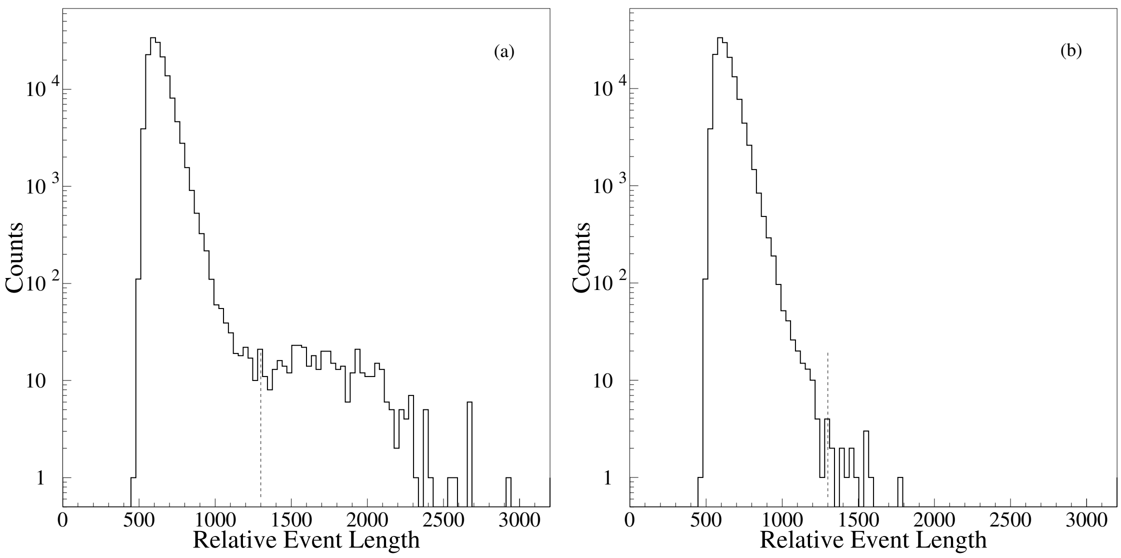

FIG. 10. The distribution of event lengths for events passing (a) the total momentum, zunin, and mass cuts and (b) the total momentum, zunin, mass, and the trigger cuts. The dashed line shows the value of the ntuple cut made on the relative length of the event.

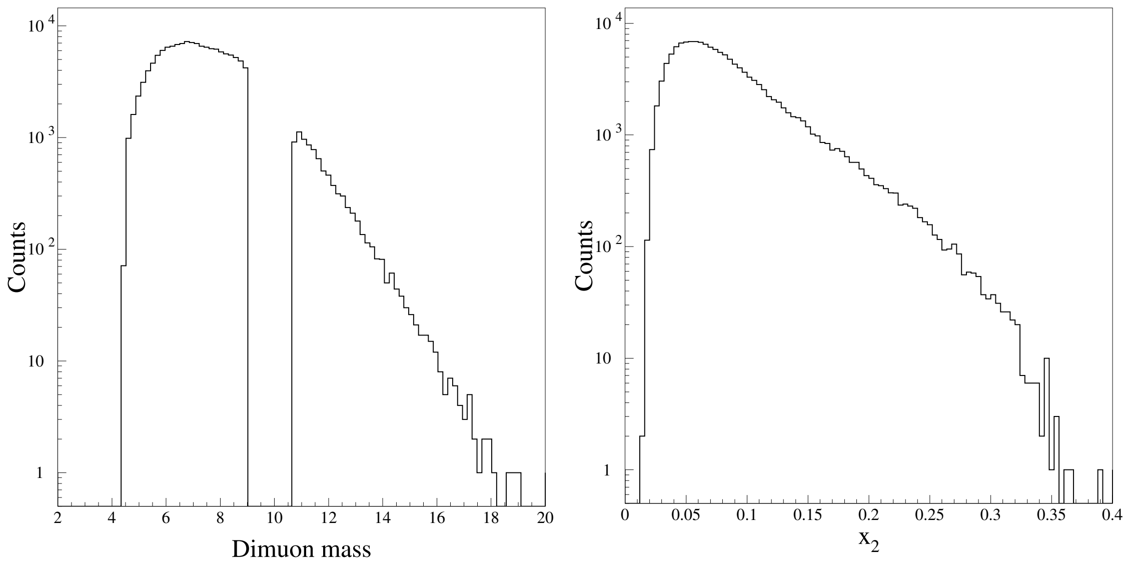

FIG. 11. The mass and x_2 distributions of events reconstructed by the second pass analysis and accepted by the ntuple cuts. The dimuon mass is in units of GeV/c^2.

B. Derivation of the cross section ratio formula

If N_h is defined as the raw numbers of events from the hydrogen target, then the following should be true,

$$N_h \;=\; I_h \cdot A_h \cdot t_h \cdot \rho_h \cdot \frac{H}{g} \cdot \frac{d\sigma^{pp}}{d\Omega} \cdot \Delta\Omega_h \cdot R_h \;+\; N_{h-junk}, \tag{4.3}$$

where N_{h-junk} is the number of events originating near the hydrogen target that were not proton-hydrogen Drell-Yan events. This "junk" from near the hydrogen target has two different origins. The majority of the "junk" events are Drell-Yan muons produced by the beam protons interacting with the target flask walls, beamline vacuum windows near the target, and material in the ME6SWIC. This source of "junk" is measured and corrected for by measuring the Drell-Yan yield off of the empty target flask, N_e. Also "junk" events can be produced by 2 unrelated, oppositely charged, random muons. The number of these random events off of the hydrogen target is defined as $N_{h-randoms}$. With this in mind the number of "junk" events off of the hydrogen target can be written as

$$N_{h-junk} \;=\; \frac{N_{e(z<0)} \;+\; \lambda_h \cdot N_{e(z>0)}}{I_e} \cdot I_h \;+\; N_{h-randoms}. \tag{4.4}$$

To express the number of events off of the deuterium target, N_d, in this way is more complicated, due to the fact that for data sets 8 and 11 the material used for the target was not pure deuterium. Mass spectrograph analyses of the target gas determined that hydrogen was the only significant contaminant present. Because of this contamination, the number of events off of the deuterium target is a function of both the proton-deuterium and proton-hydrogen Drell-Yan cross sections, as shown in,

$$N_d \;=\; I_d \cdot A_d \cdot t_d \cdot \Delta\Omega_d \cdot \left[f_h \cdot \frac{d\sigma^{pp}}{d\Omega} \;+\; f_d \cdot \frac{d\sigma^{pd}}{d\Omega} \right] \cdot \rho'_d \frac{D}{g} \cdot R_d \;+\; N_{d-junk}. \tag{4.5}$$

The N_{d-junk} term is similar to that for the hydrogen target,

$$N_{d-junk} \;=\; \frac{N_{e(z<0)} \;+\; \lambda_d \cdot N_{e(z>0)}}{I_e} \cdot I_d \;+\; N_{d-randoms}, \tag{4.6}$$

with $N_{d-randoms}$ defined as the number of random events off of the deuterium target. In the four equations above I have used the following variables:

N_h - number of hydrogen target events

N_d - number of deuterium target events

$N_{e(z<0)}$ - number of empty target events with zunin<0

$N_{e(z>0)}$ - number of empty target events with zunin>0

λ_h - the percentage of beam that hits the downstream hydrogen target window

λ_d - the percentage of beam that hits the downstream deuterium target window

I_e, I_h, I_d - integrated beam intensity on empty, hydrogen, and deuterium targets, corrected for live time

$A_h,\ A_d$ - beam attenuation correction for the hydrogen and deuterium targets

$t_h,\ t_d$ - thickness of the hydrogen and deuterium targets

ρ_h - hydrogen mass density

ρ_d' - corrected mass density of the deuterium target

$\frac{H}{g}, \frac{D}{g}$ - number of hydrogen and deuterium atoms per gram

σ^{pp} - proton hydrogen Drell Yan cross section

σ^{pd} - proton deuterium Drell Yan cross section

f_h - fraction of hydrogen atoms in deuterium target

f_d - fraction of deuterium atoms in deuterium target

$R_h,\ R_d$ - rate dependence corrections for the hydrogen and deuterium targets

$\Delta\Omega_h,\ \Delta\Omega_d$ - the spectrometer's acceptance for Drell-Yan events from the hydrogen and deuterium targets

The cross section ratio is found by first solving Eq. 4.3 and Eq. 4.5 for the hydrogen and deuterium cross sections, respectively, and then taking the ratio.

$$\frac{\sigma^{pd}}{2\sigma^{pp}} = \frac{N_d - N_{d-junk}}{N_h - N_{h-junk}} \cdot \frac{1}{2} \cdot \frac{I_h}{I_d} \cdot \frac{R_h}{R_d} \cdot \frac{A_h t_h}{A_d t_d} \cdot \frac{\rho_h \frac{H}{g}}{f_d \rho_d' \frac{D}{g}} \cdot \frac{\Delta\Omega_h}{\Delta\Omega_d} - \frac{f_h}{2 f_d} \tag{4.7}$$

The factor of 1/2 on both sides of Eq. 4.7 is a convention of the E866 collaboration. Since, to first order, σ^{pd} is expected to be twice σ^{pp}, this convention allows us to compare the cross section ratio to a baseline of unity.

TABLE IV. Results of gas analyses of the "bad" deuterium. The results shown are in percent volume.

material	target flask sample	bottle sample
D_2	93.8 ± 0.7	92.7 ± 0.8
HD	5.80 ± 0.58	6.89 ± 0.69
H_2	0.053 ± 0.011	0.147 ± 0.015
N_2	0.327 ± 0.033	0.245 ± 0.024
Ar	0.003 ± 0.002	—
CO_2	0.006 ± 0.003	0.0039 ± 0.0008

C. Normalization quantities

1. *Target compositions*

Two different qualities of deuterium gas were used to fill the liquid deuterium target. The "good" deuterium was analyzed, and found to be 99.99% pure deuterium. Two samples were taken of the "bad" deuterium used in the experiment. One sample was taken from the gas bottle used to store the deuterium, and the other sample was taken while the deuterium target flask was being emptied. The sample from the target flask was taken after about half of the deuterium in the flask had already boiled off. The analysis results of both samples are shown in Table IV. Both of these samples were taken when the "bad" deuterium was in the gas state. However when this gas was liquified to be used in the target the composition of the actual liquid was not likely the same as either gas sample. The heavier components (N_2, Ar, and CO_2) should have been frozen out of the liquid, and the lighter components (H_2 and HD) should have been somewhat "distilled" out into the gas present above the liquid in the target.

TABLE V. Best estimate of the composition of the "bad" deuterium. The results shown are in percent volume.

material	percent volume
D_2	94.05 ± 0.6
HD	5.90 ± 0.6
H_2	0.05 ± 0.01

TABLE VI. Pressures in psi of the liquid targets for each of the high mass data sets.

	hydrogen	deuterium
data set 7	15.06 ± 0.13	14.98 ± 0.14
data set 8	15.11 ± 0.06	15.17 ± 0.06
data set 11	15.15 ± 0.05	15.21 ± 0.04

Considering how and when the samples were taken, the sample taken while the target flask was being emptied is a slightly more accurate description of the liquid in the target. Taking all of this into consideration the best estimate of the contents of the "bad" deuterium is given in Table V. From these values it is clear that $3.0\% \pm 0.6\%$ of the nuclei in the "bad" deuterium are hydrogen, and the other $97.0\% \mp 0.6\%$ are deuterium.

The vapor pressure of the gas above the liquid in both targets was constantly monitored and recorded in a database. These pressures were also recorded on the shift checks. From the shift check readings, the average pressure and its statistical uncertainty was determined for each target and for each data set. These pressures are shown in Table VI.

TABLE VII. Densities in g/cm^3 of the liquid targets for each of the high mass data sets.

	hydrogen	deuterium
data set 7	0.07069	0.16277
data set 8	0.07068	0.16266
data set 11	0.07067	0.16263

Cryogenic data tables [18] for hydrogen and deuterium were used to derive formulas for converting vapor pressure (in psi) to mass density (in g/cm^3) for both targets. It was assumed that the hydrogen target contained pure para-hydrogen within 36 hours of the target being filled. For liquid para-hydrogen, the relation between vapor pressure and density is

$$\frac{1}{\rho_h} = 62.473\left(0.2115 + 0.1171\times 10^{-2}P - 0.1109\times 10^{-4}P^2\right), \tag{4.8}$$

where P is the pressure in psi. The formula for pure deuterium is

$$\rho_d = 4.028\times 10^{-3}\left(43.291 - 3.4176\frac{P}{14.6959} + 0.5783\left(\frac{P}{14.6959}\right)^2\right). \tag{4.9}$$

The coefficients for these two formulas have been adjusted to give the correct units. From the pressures and equations above, the densities shown in Table VII were calculated. The "bad" deuterium also had a slightly different density of nuclei than the "good" deuterium because of the contaminants. In the liquid state an H_2 molecule is approximately 12.8% larger than a D_2 molecule, and an HD molecule is approximately 8.6% larger [18]. Therefore, relative to pure D_2, the volume of the "bad" deuterium is

$$V_c \;=\; 0.9405 \times 1.00 \;+\; 0.0590 \times 1.086 \;+\; 0.0005 \times 1.128 \;=\; 1.005 \pm 0.001. \quad (4.10)$$

The density of nuclei in the "bad" deuterium is modified by this correction factor,

$$\rho_d' \frac{D}{g} \;=\; \frac{1}{V_c} \rho_d \frac{D}{g}. \quad (4.11)$$

2. *Rate dependence*

The efficiency with which events were detected, and later reconstructed in the analysis, was dependent in part on two quantities, the instantaneous beam intensity and the interaction length of the target. These two quantities largely determined the number of charged particles going through the spectrometer at any one time. Rate dependence is defined as the degree with which the efficiency of the detection and reconstruction of events is dependent on the magnitude of the flux of the charged particles going through the spectrometer. Rate dependence in E866 was caused by limitations of the spectrometer and DAQ hardware and the analysis software. Because the drift chamber TDCs utilized "single hit" electronics, if two charged particles had hit the same drift cell during an event, the position information about one of those particles was lost. This loss of information may have made the event impossible to reconstruct later during analysis. Entire events may have also been lost due to "dead time". It took a relatively long time (10 μs or more) compared to the time between beam buckets for the DAQ to collect and record to tape all of the data for an event. While the DAQ was busy collecting and recording data, the trigger system was disabled and any events that occurred during this time were lost due to system "dead time". Events may have been lost also during reconstruction in analysis. If there were too many doublets and triplets in the wire chambers, the analysis program would have been unable to match them together to form a track, and the event would be discarded. Since the deuterium target had half the interaction length of the hydrogen target, rate dependence effects were larger for deuterium data than the hydrogen data.

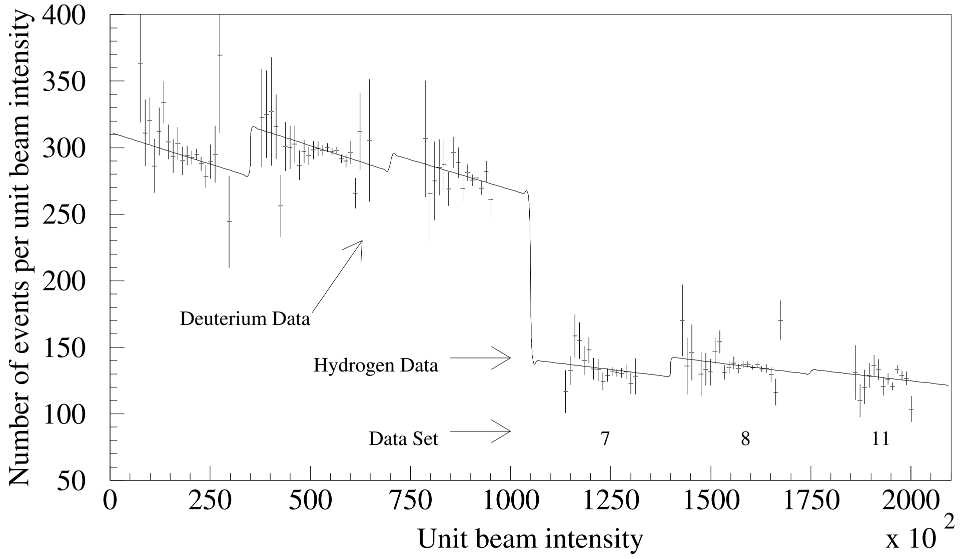

FIG. 12. The rate dependence is shown for both the hydrogen and dueterium targets for the three high mass data sets.

The rate dependence for both the hydrogen and deuterium targets was measured by plotting the number of reconstructed events per unit beam intensity versus the beam intensity of the spill during which the events were detected. For both targets the number of events per unit beam intensity decreases as the beam intensity increases, as can be seen in Fig. 12. This figure also shows that rate dependence for deuterium events is slightly larger than that for hydrogen events. The ratio of these two rate dependences was measured to be

$$\frac{R_h}{R_d} = 1.0123 \pm 0.0062. \tag{4.12}$$

Evidence that the rate dependence was different for hydrogen and deuterium was also seen in the number of drift chamber hits in events. After the hits due to the dimuon were subtracted from events, it was seen that events from the deuterium target had approximately 30% more extra drift chamber hits than events from the hydrogen target.

3. *Beam attenuation*

As the proton beam traveled through the target it was attenuated by beam-target interactions. Because the densities of the two targets were different, the beam was attenuated by different amounts in the two targets. Since the deuterium target was denser than the hydrogen target, the beam was attenuated more in the deuterium, and fewer beam protons were left to produce Drell-Yan interactions. By using the proton-proton and proton-deuteron cross sections [19], and the density measurements shown previously, it was determined that for the "good" deuterium, the ratio of attenuation factors was

$$\frac{A_h}{A_d} = 1.042 \pm 0.002, \tag{4.13}$$

and for the "bad" deuterium, the attenuation correction was

$$\frac{A_h}{A_d} = 1.040 \pm 0.002. \tag{4.14}$$

The uncertainties shown for the attenuation corrections are systematic.

The acceptance for events from the hydrogen and deuterium targets may not have been identical. Even though the two targets were the same size and the targets were in the same position when they were hit by the beam, the two liquid targets had different acceptances due to the different amounts of attenuation in the two targets. This difference in beam attenuation caused the mean interaction point for the two targets to be different. Monte Carlo studies have shown that the acceptance for high mass dimuon events is sensitive to the z position of the event vertex. The difference in the acceptances of the targets has not yet been able to be measured by Monte Carlo methods, and was not seen in the data. Therefore, I will assume that the acceptance for events from the two liquid targets was identical to within a systematic uncertainty of 0.7%, as suggested by the Monte Carlo results to date.

4. *Background subtraction*

The largest source of background dimuon events for the experiment was from beam protons interacting with the walls and vacuum windows of the target flasks or other materials near the targets, such as beamline vacuum windows or the ME6SWIC. As shown in Eq. 4.4 and Eq. 4.6, these sources of background events were corrected for by subtracting the empty target Drell-Yan yield from the hydrogen and deuterium yields. For the correction to both targets the empty target Drell-Yan yield was renormalized to the same integrated beam intensity as the liquid target being corrected. An example of this has already been shown in Fig. 9. This background subtraction was approximately a 6% correction to the number of deuterium target events, and approximately a 13% correction to the number of hydrogen target events. Because of beam attenuation in the liquid targets, the fraction of the beam hitting the downstream target flask wall and vacuum window was different for all three targets. Even though the difference in beam attenuations had a small effect on the empty target subtraction, it was corrected for by weighting the events from the downstream end of the target (zunin>0) by an attenuation factor.

As mentioned previously, another source of background events was random muons. Since single muons of either charge can be produced in beam-target interactions, it was possible for two oppositely charged muons to be produced at the target, but not due to a Drell-Yan process. These random events were studied as follows. Events with two muons with the same charge were triggered on if the two muons were on opposite sides of x=0. The probability of this type of event occurring is related to the probability for a random event to occur with oppositely charged muons, and with each muon on opposite sides of x=0. Another trigger was used to select events with only one muon originating from the target. By combining these single muon events together in pairs, a distribution was made versus x for events with two random muons. The random event distribution from the single muon events was subjected to the same cuts as the real data, and was normalized to give the same rate of same sign, opposite side events as observed by the trigger mentioned above. After these cuts and normalization, the randoms distribution was subtracted from the raw number of events, as shown in Eq. 4.4 and Eq. 4.6. This correction was small, averaging 0.2% over the x range of the data. The process of measuring the randoms background was done separately for both the hydrogen and the deuterium targets. There were no same sign, opposite side events from the empty target that passed the analysis cuts, so it was assumed the events from this target were free of randoms background.

D. The cross section ratio

A fortran program was used to combine the event and normalization information described above into the ratio of Drell-Yan cross sections, $\sigma^{pd}/2\sigma^{pp}$, versus the x of the target parton. The data from each of the three high mass data sets was stored in its own ntuple file. The fortran program read through each of these ntuples event by event, and subjected each event to the set of cuts discussed earlier in this chapter. Once an event passed all of the cuts, the event was sorted by target, data set, and the value of x_2. For each data set and target, there was an x_2 array of eleven bins. Each bin stored the number of events with an x_2 value that was within the x_2 range

TABLE VIII. The average values for kinematic variables in each x_2 bin.

x_2 range min-max	$< x_2 >$	$< x_F >$	$< p_T >$ (GeV/c)	$< M_{\mu^+\mu^-} >$ (GeV/c^2)
0.02-0.045	0.036	0.537	0.92	5.5
0.045-0.070	0.057	0.441	1.03	6.5
0.070-0.095	0.082	0.369	1.13	7.4
0.095-0.120	0.106	0.294	1.18	7.9
0.120-0.145	0.132	0.244	1.21	8.5
0.145-0.170	0.156	0.220	1.21	9.3
0.170-0.195	0.182	0.192	1.20	9.9
0.195-0.220	0.207	0.166	1.19	10.6
0.220-0.245	0.231	0.134	1.18	11.1
0.245-0.295	0.264	0.095	1.18	11.8
0.295-0.345	0.312	0.044	1.12	12.8

of that bin. The number of bins, as well as the x_2 ranges for the bins, were chosen so that gaussian statistics could be reliably used when combining data sets. Table VIII shows the average values for x_2, x_F, p_T, and mass for each bin. Figure 13 shows the x_1, x_2 distribution for both Drell-Yan and Υ events.

The beam intensity for each spill was also read from the ntuples. The beam intensity monitor that was used (SEM6) had a small but finite offset from zero; this offset was approximated by looking at the SEM6 output from spills with no beam. The offset was found to vary slowly over time, and so time dependent offsets were used for the high mass data set. After this offset was subtracted, the beam intensity was summed for each target in each data set.

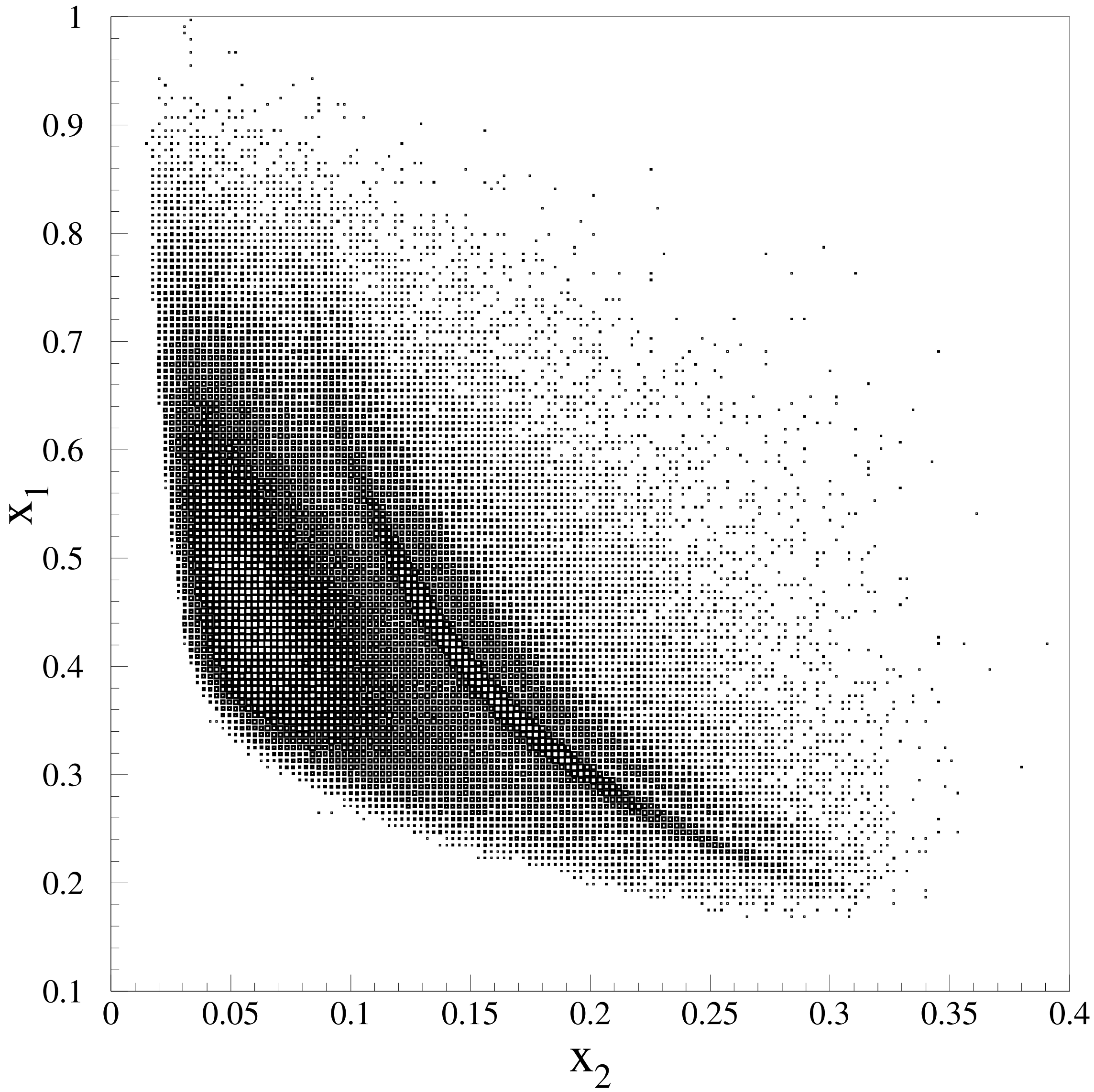

FIG. 13. The correlation between x_1 and x_2 for events. All analysis cuts were used except for the Υ mass cut.

The number of events due to random muons was computed separately for each x_2 bin for each target and data set, and was read into the fortran program from a series of data files. The normalization factors for beam attenuation, target density, rate dependence, and the correction term for the "bad" deuterium were all stored in the program. For each x_2 bin, the ratio of cross sections was computed separately for each data set, as shown in Eq. 4.7. The statistical error for each ratio measurement was calculated, assuming that the uncertainty in the number of events obeyed gaussian statistics. The three measurements (one for each data set) of the cross section ratio in each x_2 bin were combined, along with their errors, to give one ratio result for the bin. If, in a given x_2 bin, r_i was the ratio measured in the ith data set with a statistical uncertainty of δ_i, then the total cross section ratio R with a statistical uncertainty Δ for that bin was found by

$$R \pm \Delta = \frac{\sum_i r_i \cdot \frac{1}{\delta_i^2}}{\sum_i \frac{1}{\delta_i^2}} \pm \left(\frac{1}{\sum_i \frac{1}{\delta_i^2}} \right)^{1/2}. \tag{4.15}$$

The fortran program output its results in the form of both a histogram, and a table as shown in Fig. 14, and Table IX. The data points in Fig. 14 are plotted at the center of each x_2 bin. However, this can be misleading since the average value of x_2 for all the events in a bin is not necessarily at the center of the bin, as seen in Table VIII.

E. Systematic uncertainties in the cross section ratio

Several systematic effects in the experiment influenced both the hydrogen and the deuterium data essentially equally. Some of these effects included changes in detector efficiency due to temperature variations, changes in beam angle and position at the

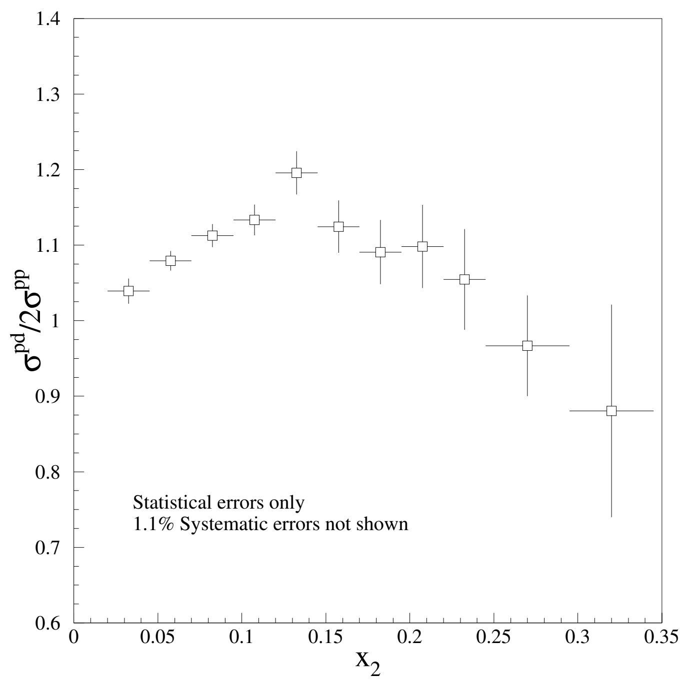

FIG. 14. The ratio of Drell-Yan cross sections is shown versus the x of the target parton.

target, and changes in the relative phase between the beam and the RF clock. Since it was the ratio of the cross sections that was desired, many potentially large sources of systematic errors canceled because they equally affected the data from both liquid targets. The sources of systematic uncertainties that were not ignored are listed in Table X along with their uncertainties.

The sources of many of these systematic uncertainties have previously been discussed in this chapter. The uncertainty in the target length comes from the fact that we do know how much the two liquid target flasks differ in length, but we do not know which target was the longer flask. By adding all of the uncertainties listed in Table X in quadrature, the total systematic uncertainty of the cross section ratio was found to be $\approx 1.1\%$.

TABLE IX. The cross section ratio calculated for each data set and the final result for each x_2 bin.

x_2 range	$\sigma^{pd}/2\sigma^{pp}$			
min-max	data set 7	data set 8	data set 11	final result
0.020-0.045	1.034 ± 0.033	1.042 ± 0.022	1.038 ± 0.041	1.039 ± 0.017
0.045-0.070	1.053 ± 0.024	1.094 ± 0.018	1.076 ± 0.032	1.079 ± 0.013
0.070-0.095	1.115 ± 0.030	1.105 ± 0.020	1.140 ± 0.039	1.113 ± 0.015
0.095-0.120	1.106 ± 0.039	1.157 ± 0.028	1.105 ± 0.047	1.133 ± 0.020
0.120-0.145	1.173 ± 0.053	1.209 ± 0.039	1.193 ± 0.070	1.196 ± 0.029
0.145-0.170	1.133 ± 0.069	1.122 ± 0.046	1.119 ± 0.081	1.124 ± 0.035
0.170-0.195	1.109 ± 0.082	1.133 ± 0.060	0.973 ± 0.091	1.091 ± 0.043
0.195-0.220	1.081 ± 0.100	1.195 ± 0.082	0.945 ± 0.110	1.098 ± 0.055
0.220-0.245	0.972 ± 0.125	1.060 ± 0.086	1.230 ± 0.194	1.055 ± 0.067
0.245-0.295	0.817 ± 0.101	1.099 ± 0.103	1.035 ± 0.176	0.967 ± 0.067
0.295-0.345	0.806 ± 0.275	0.855 ± 0.176	1.242 ± 0.445	0.881 ± 0.141

TABLE X. Systematic uncertainties and their sources.

source of uncertainty	uncertainty
rate dependence	0.6 %
target length	0.2 %
beam intensity	0.1 %
beam attenuation	0.2 %
"bad" deuterium composition	0.6 %
"bad" deuterium density	0.1 %
acceptance differences	0.7 %

CHAPTER V

THE EXTRACTION OF $\bar{d}(x)/\bar{u}(x)$ FROM THE RATIO OF CROSS SECTIONS

As discussed in the last section of chapter I, the ratio of Drell-Yan cross sections measured by E866 is strongly dependent on the ratio $\bar{d}(x_2)/\bar{u}(x_2)$ as shown in the equation

$$\left.\frac{\sigma^{pd}}{\sigma^{pp}}\right|_{x_1>>x_2} \approx \frac{1 + d_1/4u_1}{1 + (d_1/4u_1)\cdot(\bar{d}_2/\bar{u}_2)}\left(1 + \frac{\bar{d}_2}{\bar{u}_2}\right). \tag{5.1}$$

If this equation is used as a guide, then the cross section ratio measured by E866 as a function of x_2, as shown in Fig. 14, is an indication of a significant $\bar{d}/\bar{u}$ asymmetry in the proton. The cross section ratio can be plotted as functions of kinematic variables other than x_2, as seen in Fig. 15, however in these forms the ratio is less sensitive to a flavor asymmetry. In order to perform a more precise extraction of the $\bar{d}/\bar{u}$ asymmetry from the cross section ratio, a more complicated calculation is needed than what is suggested by Eq. 5.1. This determination of the $\bar{d}/\bar{u}$ asymmetry is the subject of this chapter.

The basic philosophy for calculating the $\bar{d}/\bar{u}$ asymmetry was to use existing PDF parametrizations to calculate the ratio of Drell-Yan cross sections and then to vary $\bar{d}(x)/\bar{u}(x)$ until the calculated cross section ratio agreed with the values measured by E866. The PDF parametrizations used were CTEQ4M [12] and MRS(R2) [20]. Because experiments previous to E866 have provided data on $\bar{d}(x)+\bar{u}(x)$ in the proton that have been included in the existing PDF parametrizations, this quantity was kept constant while $\bar{d}(x)/\bar{u}(x)$ was varied during the calculation. Keeping $\bar{d}(x) + \bar{u}(x)$ constant also guaranteed that the momentum conservation of the parametrization

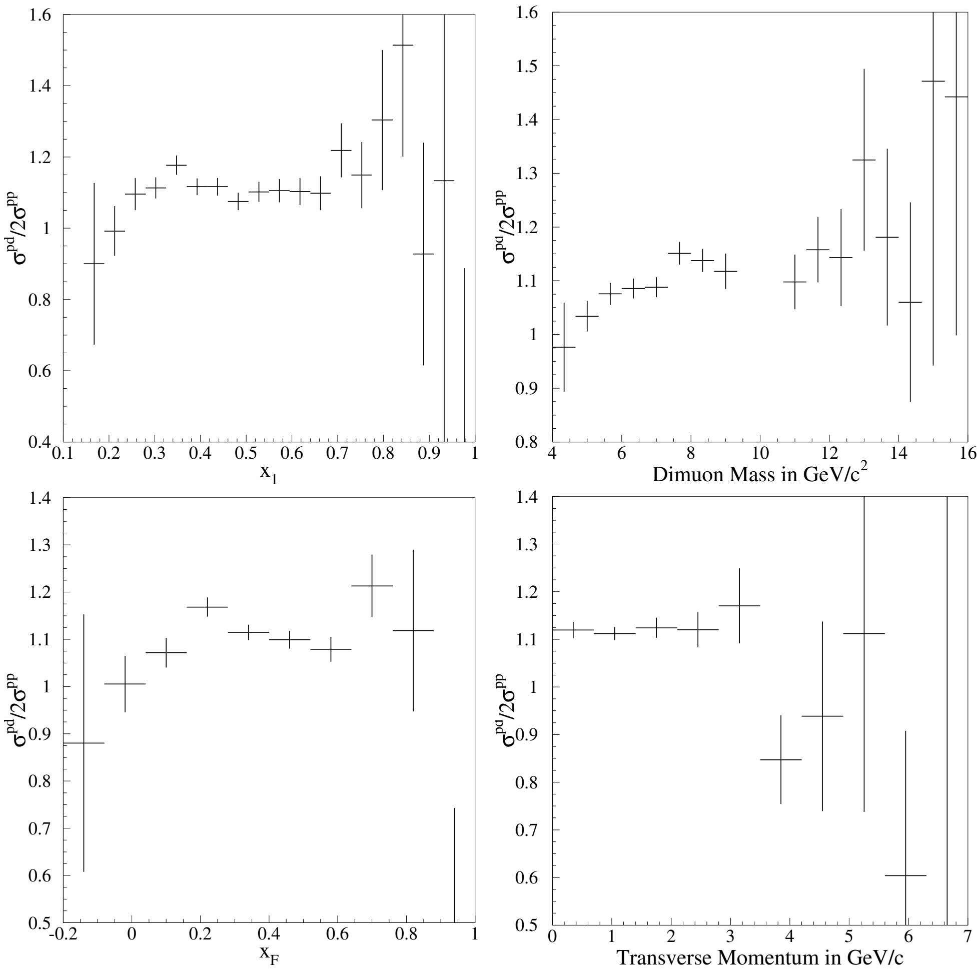

FIG. 15. The ratio of Drell-Yan cross sections as functions of x_1, mass, x_F, and p_T.

was preserved, meaning that the following equation will always be true.

$$\int_0^1 \sum_i x q_i(x) dx \;=\; 1 \tag{5.2}$$

Values from a PDF parametrization were used as initial input values for $\bar{d}(x)/\bar{u}(x)$. Then an iterative procedure was used to calculate $\bar{d}(x)/\bar{u}(x)$. The full leading order Drell-Yan cross section formula, including all quark flavors but the top quark, was used to calculate the cross section ratio as a function of x_2 for the given $\bar{d}(x)/\bar{u}(x)$

ratio. In the cross section calculation, the up and down sea quark distributions were defined by the chosen values of $\bar{d}(x)/\bar{u}(x)$, the values of $\bar{d}(x)+\bar{u}(x)$ given by the PDF parametrization, and the assumption that the $\bar{d}(x)/\bar{u}(x)$ ratio was unity outside the range of x_2 measured by E866. The PDFs for the up and down valence quarks and the strange, charm, and bottom sea quarks and antiquarks were all supplied by the PDF parametrization used for the calculation. In order to account for acceptance effects in the measured cross section ratio, the cross section ratio was calculated for the x_1, x_2, and Q^2 values for every event that passed the analysis cuts. The average of the calculated cross section ratios was found for each x_2 bin. The same set of bins was used in the $\bar{d}/\bar{u}$ calculation as was used in the measured cross section ratio. In each of these x_2 bins, the calculated and measured cross section ratios were compared, and a new $\bar{d}(x_2)/\bar{u}(x_2)$ ratio was calculated using the equation

$$\left[\frac{\bar{d}(x_2)}{\bar{u}(x_2)}\right]_{new} = \Delta\sigma\left(1+\left[\frac{\bar{d}(x_2)}{\bar{u}(x_2)}\right]_{old}\right) - 1, \tag{5.3}$$

where the term $\Delta\sigma$ is the ratio of measured to calculated cross section ratios. Equation 5.3 is derived from a simplified version of Eq. 5.1. The difference between the calculated cross section ratios from successive iterations was summed over all x_2 bins. When this sum was less than 0.001 the calculation was assumed to have converged on a final result for $\bar{d}(x)/\bar{u}(x)$. Otherwise the calculation was repeated using the new set of $\bar{d}/\bar{u}$ ratios to calculate a new cross section ratio.

Unlike the values of $\bar{d}/\bar{u}$ obtained from PDF parametrizations, the new values of $\bar{d}/\bar{u}$, as defined by Eq. 5.3, did not vary across an x_2 bin. While this detail would not affect the calculation significantly in most x_2 bins, it was a factor in the bins at high x_2 where $\bar{d}/\bar{u}$ was changing rapidly compared to the width of the bin. In order to more accurately represent the $\bar{d}/\bar{u}$ ratio at all values of x_2, an approximate uncertainty was calculated for each new $\bar{d}/\bar{u}$ ratio, and the points were fit with a simple 4th order polynomial. However, if this smooth curve was used for $\bar{d}(x)/\bar{u}(x)$ in the calculation, then each iteration would artifically remove some of the statistical fluctuation of the data. In an attempt to keep the scatter in the data, the fitted curve was moved, or "offset", within each x_2 bin so that the curve went through the $\bar{d}/\bar{u}$ value at the average x_2 for that bin. An example of this "offset" curve can be seen in Fig. 16 along with the values of $\bar{d}/\bar{u}$ as calculated by Eq. 5.3. This "offset" curve was the $\bar{d}(x)/\bar{u}(x)$ function used in the next iteration of the calculation.

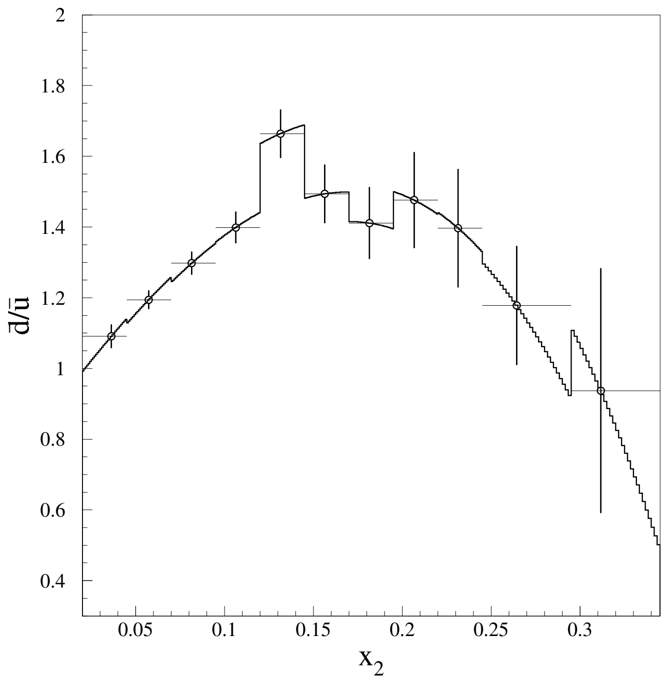

FIG. 16. An "offset" curve used in the $\bar{d}/\bar{u}$ calculation along with the $\bar{d}/\bar{u}$ values for each bin.

Because the measured cross section ratio is largely insensitive to changes in $\bar{d}(x_1)/\bar{u}(x_1)$, when the value of x_1 for an event was less than 0.345 the value of $\bar{d}(x_1)/\bar{u}(x_1)$ used in the cross section ratio calculation was obtained from the smooth fit to the $\bar{d}/\bar{u}$ points. However, since the event in question and the corresponding point on the smooth fit used for the cross section ratio calculation can have different values of Q^2, this method is not exactly correct. The effect of this inconsistency is small because the ratio $\bar{d}(x)/\bar{u}(x)$ at a fixed value of x varies slowly over the range of Q^2 for the data. This problem was not present during the next-to leading order calculation of $\bar{d}/\bar{u}$, which will be discussed later in this chapter.

When the value of x_1 for an event was greater than 0.345, it was assumed that $\bar{d}(x_1)/\bar{u}(x_1)$ was a constant. It was found that the $\bar{d}(x)/\bar{u}(x)$ results were largely insensitive to the value of the constant used for $\bar{d}(x_1)/\bar{u}(x_1)$ at large x_1 ($x_1 > 0.345$). The results from using three different values of this constant are compared in Fig. 17. The final $\bar{d}/\bar{u}$ calculation assumed that $\bar{d}(x_1)/\bar{u}(x_1)$=1.00 at large x_1.

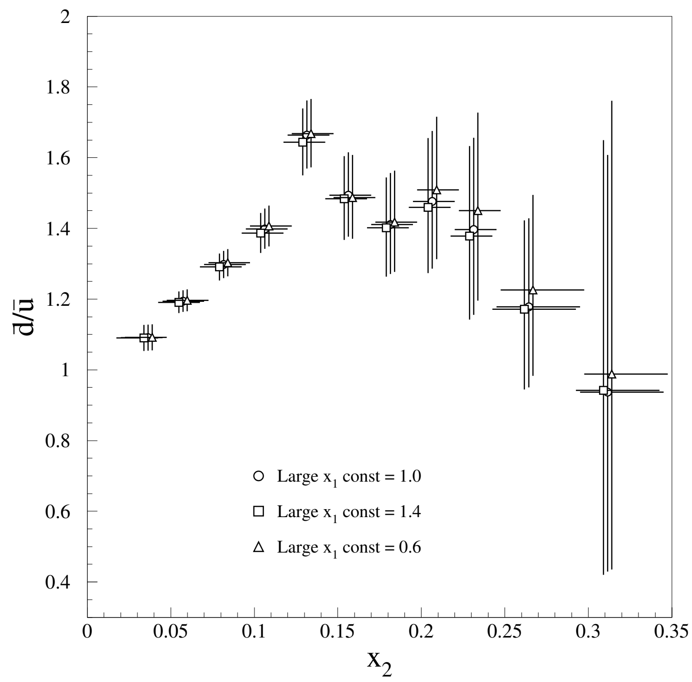

FIG. 17. A comparison of the calculated $\bar{d}/\bar{u}$ results found using different constants for $\bar{d}(x_1)/\bar{u}(x_1)$ at large x.

The uncertainty used for each $\bar{d}(x)/\bar{u}(x)$ point during the calculation was only an estimate of the real uncertainty for those points. After the iteration process had converged on the final values for $\bar{d}(x)/\bar{u}(x)$, the statistical uncertainty for these points was calculated from the statistical uncertainty of the measured cross section ratio. This was done by moving a single x_2 point of the measured cross section ratio one standard deviation higher (or lower) than its true position. Then the iterative calculation was repeated with this modified cross section ratio, and the result was a value for $\bar{d}/\bar{u}$ for this x bin one standard deviation higher (or lower) than its true value. This method was used to calculate the statistical uncertainty for all of the $\bar{d}/\bar{u}$ points. Because of the procedure used to keep the statistical fluctuations of $\bar{d}/\bar{u}$ intact during the calculation, there was relatively little contribution to the uncertainty in one bin from the uncertainties in all the other bins. When the correlations between the uncertainties of all of the bins was accounted for the uncertainty increased by an average of less than 1.5%.

Most of the sources of systematic uncertainties for the cross section ratio were independent of both x_1 and x_2. Because of this their contribution to the systematic uncertainty of $\bar{d}/\bar{u}$ was calculated simply by raising (lowering) the measured cross section ratio results in all x_2 bins by one systematic standard deviation. The resulting $\bar{d}(x)/\bar{u}(x)$ was then one systematic standard deviation higher (lower) than its true value. By using this method a systematic uncertainty of 0.032 was found for all x bins.

The contribution to the systematic uncertainty from the PDF parametrization used in the $\bar{d}/\bar{u}$ calculation was also investigated. Even though there are no uncertainties quoted for the PDF parametrizations, an estimate can be made of the systematic uncertainty due to PDF parametrization by simply performing the $\bar{d}/\bar{u}$ calculation with different PDF parametrizations and comparing the results. From the comparison of the CTEQ4M and MRS(R2) results shown in Fig. 18 it can be seen that the uncertainty due to the PDF parametrization is quite small compared to the 0.032 systematic uncertainty described above.

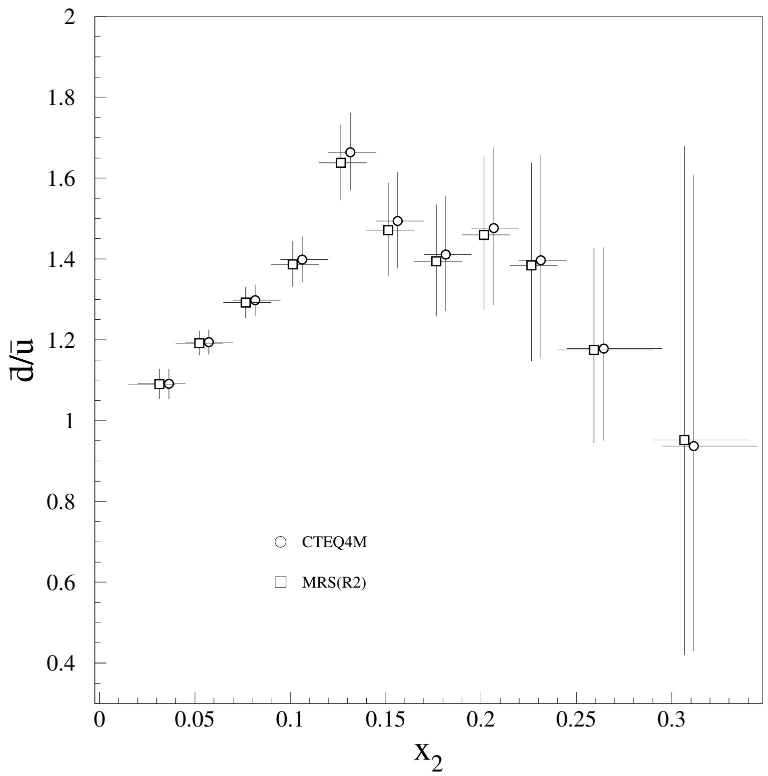

FIG. 18. A comparison between $\bar{d}/\bar{u}$ results obtained by using CTEQ4M and MRS(R2) in the calculation.

In addition to the leading order electromagnetic process there are two classes of Feynman diagrams that contribute to the Drell-Yan cross section to $\mathcal{O}(\alpha_s)$. The contributions from the diagrams shown in Fig. 19(b) and Fig. 19(c) have a similar dependence on the quark and antiquark PDFs as the electromagnetic leading order diagram shown in Fig. 19(a), so they are expected to produce very little change in the calculation of the ratio of Drell-Yan cross sections as a function of x_1 and x_2 when they are included. The other class of diagrams, shown in Fig. 19(d) and Fig. 19(e), should effect both the proton-neutron and the proton-proton Drell-Yan cross sections equally in the large x_F limit because the gluon distributions for the proton and neutron are basically the same. There are two other diagrams not shown that are similar to Fig. 19(d) and Fig. 19(e), but have initial and final state antiquarks instead of quarks.

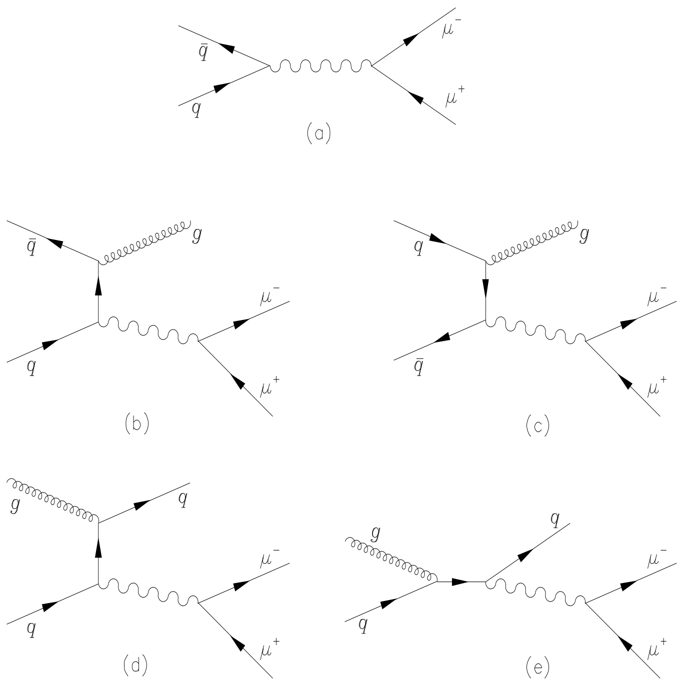

FIG. 19. Feynman diagrams of $\mathcal{O}(\alpha_s)$ or less which contribute to the Drell-Yan cross section.

The full next-to-leading order (NLO) Drell-Yan cross section is computed by including the contributions from all the diagrams shown in Fig. 19. Through the gracious cooperation of W.K. Tung, the E866 experiment obtained from the CTEQ collaboration the computer code which they use to calculate NLO Drell-Yan cross sections. This code was used with the CTEQ4M parametrization to calculate the NLO Drell-Yan cross section ratio predicted by CTEQ and weighted by the E866 acceptance. The difference between the leading order and the NLO cross section ratios calculated with the CTEQ4M parametrization is shown in Fig. 20 along with the E866 data. When the same comparison between leading and NLO calculations was made with a modified version of the CTEQ4M parametrization that set $\bar{d}(x) = \bar{u}(x) = [\bar{d}(x) + \bar{u}(x)]/2$, the resulting cross section ratios were essentially identical. Because of the small differences found in these two comparisons only the leading order cross section was used to calculate $\bar{d}/\bar{u}$.

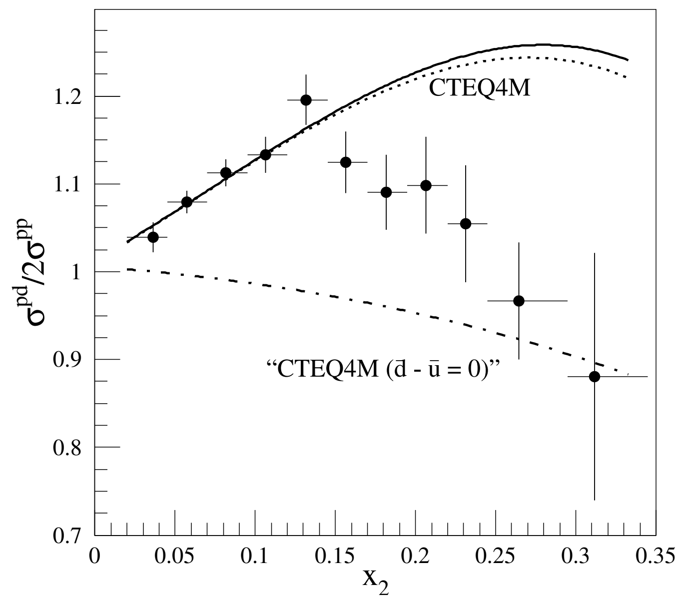

FIG. 20. A comparison between the leading order (dotted) and next-to-leading order (solid) cross section ratios as predicted by CTEQ4M. Also shown is the cross section ratio (dashed-dotted) calculated using a CTEQ4M parametrization which has been adjusted so that $\bar{d}(x) = \bar{u}(x)$.

By using the calculated values of $\bar{d}(x)/\bar{u}(x)$ and the values of $\bar{d}(x) + \bar{u}(x)$ given by a PDF parametrization, the quantity $\bar{d}(x) - \bar{u}(x)$ was calculated. As mentioned previously the average Q^2 is different for each x bin of the calculated $\bar{d}/\bar{u}$ ratio. In order to compare the E866 results to the NMC results, the integral over $\bar{d}(x) - \bar{u}(x)$ must be done with a fixed Q^2 which does not vary from bin to bin. The results in each x bin were scaled to a common fixed Q of 7.35 GeV, which is the average Q of the E866 data. The scaling factor used for each bin was computed using a PDF parametrization and calculating the ratio of a quantity ($\bar{d}/\bar{u}$ or $\bar{d}-\bar{u}$) at $Q = 7.35$ GeV to the same quantity at the variable Q of the bin. One calculation was done with $\bar{d}(x)/\bar{u}(x)$ and $\bar{d}(x)+\bar{u}(x)$ values having the same variable Q values for each x bin, and the resulting $\bar{d}(x)-\bar{u}(x)$ values, also with variable Q, were then scaled to a fixed Q. Another calculation was done, to check the results of the first, where the values of $\bar{d}(x)/\bar{u}(x)$ were scaled to a fixed Q of 7.35 GeV for all x bins, and then $\bar{d}(x)-\bar{u}(x)$ was calculated at the fixed Q. Both calculations produced nearly identical results, one of which is shown in Fig. 21.

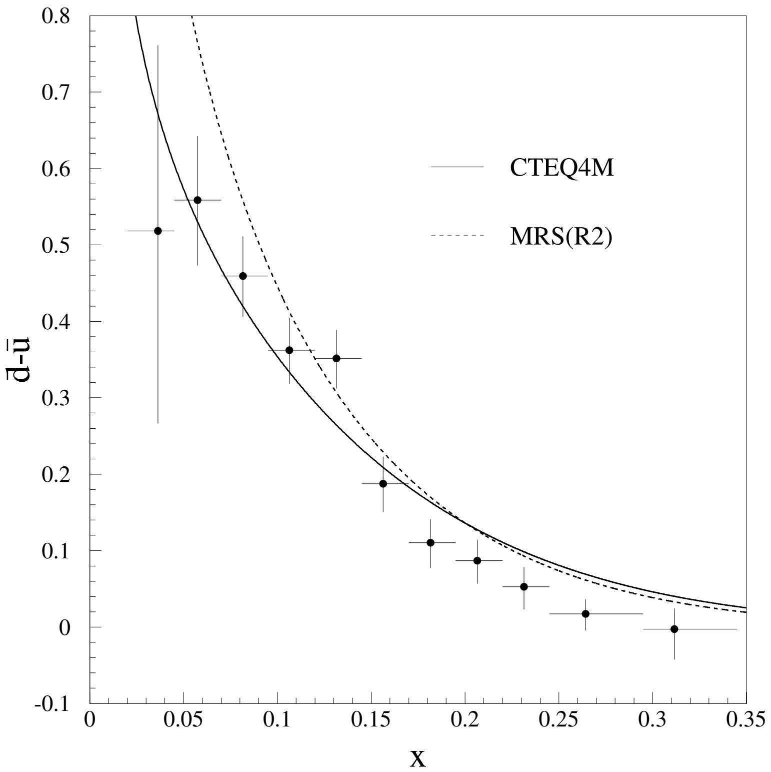

FIG. 21. $\bar{d}-\bar{u}$ as a function of x at a common Q of 7.35 GeV.

CHAPTER VI

DISCUSSION OF RESULTS AND CONCLUSION

Prior to the E866 experiment, the findings of the NA51 and NMC experiments indicated that a flavor asymmetry in the nucleon sea existed, but revealed little about its structure. So when the authors of structure function parametrizations used these new findings in their global fits to create proton models, they could only make an educated guess at the x dependence of the sea asymmetry. Nonperturbative nucleon sea production models were also used in an attempt to predict the x dependence of this asymmetry. As shown in the previous chapter, the E866 experiment has made the first measurement of the x dependence of the up-down flavor asymmetry in the nucleon sea in terms of both $\bar{d}/\bar{u}$ and $\bar{d}-\bar{u}$. In this chapter, these asymmetry results from E866 will be compared to several PDF parametrizations, models, and the NMC and NA51 results.

A. PDF parametrizations and previous experimental results

The E866 results for $\bar{d}(x)/\bar{u}(x)$ are compared to both the CTEQ4M and MRS(R2) PDF parametrizations in Fig. 22. It is interesting to note that for values of x of 0.15 and lower, both parametrizations are in reasonable agreement with the E866 results. However, for values of x of 0.20 and higher the E866 results decrease towards unity, while both the CTEQ4M and MRS(R2) parametrizations continue to increase. Also shown in Fig. 22 is the comparison between the E866 and NA51 results for $\bar{d}/\bar{u}$. While it is obvious from the figure that the E866 results are quite a bit lower than the NA51 findings, a more quantitative statement can be made if the E866 results are fit with a smooth curve. The fit shown in Fig. 22 is with the function $1 + 1120x^{2.75}(1-x)^{15}$. When this curve is compared to the NA51 result, the curve is found to be $\approx$ 2 standard deviations below the NA51 result, based on the the NA51 uncertainty. While the average Q^2 is different for the NA51 and E866 results, the change in $\bar{d}(x)/\bar{u}(x)$ due to this difference is predicted to be small by the PDFs.

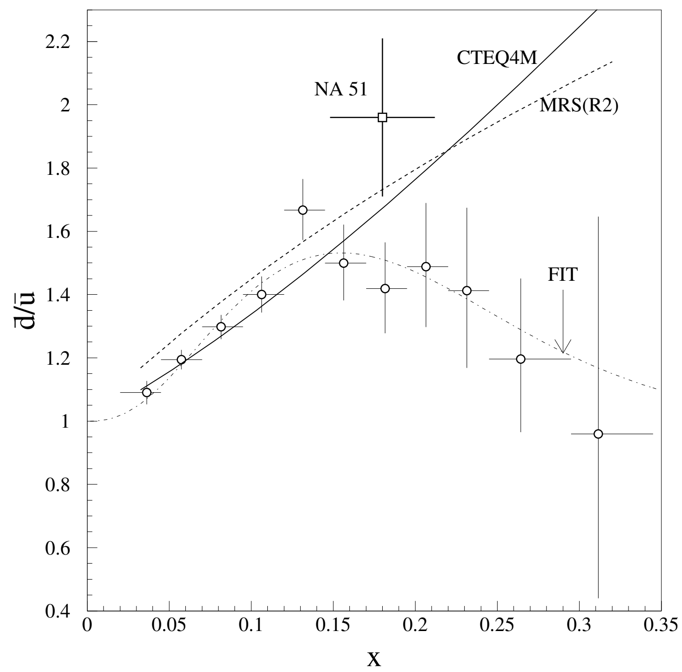

FIG. 22. A comparison of the E866 results for $\bar{d}(x)/\bar{u}(x)$ at $Q = 7.35$ GeV to the CTEQ4M and MRS(R2) predictions at the same Q. Also shown is the fit mentioned in the text and the NA51 result.

The E866 results for $\bar{d}(x) - \bar{u}(x)$ can also compared to the predictions of both the CTEQ4M and MRS(R2) parametrizations as shown in Fig. 21 and again in Fig. 23(a). The CTEQ4M parametrization gives a prediction which is in reasonable agreement with the E866 results at lower values of x, but is significantly higher than the E866 results at larger x. The prediction made by the MRS(R2) parametrization is significantly higher than the $\bar{d}(x) - \bar{u}(x)$ results from E866 both for values of x higher than 0.18, and for the lowest x bins, below an x of 0.07.

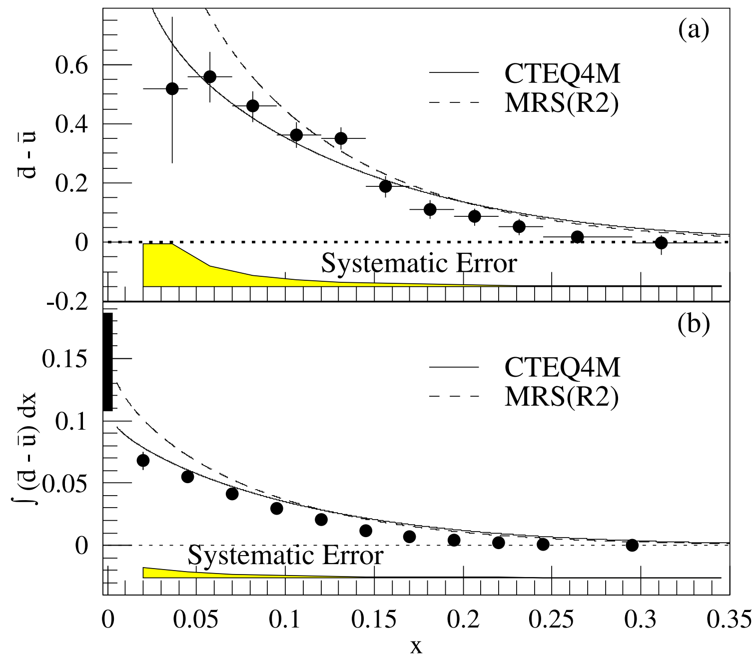

FIG. 23. A comparison of the E866 results for (a) $\bar{d}(x) - \bar{u}(x)$ and (b) $\int_x^{0.345} \bar{d}(x') - \bar{u}(x')dx'$ at $Q = 7.35$ GeV to the CTEQ4M and MRS(R2) predictions at the same Q. The bar at 0.147±0.39 on the left axis in (b) shows the result obtained for the integral from 0 to 1.

In order to compare the E866 results for $\bar{d} - \bar{u}$ to the NMC result for the Gottfried Sum, an integral over the full range of x is needed. Figure 23(b) shows the value of the integral of $\bar{d} - \bar{u}$ from E866 between x and 0.345 as a function of x. When this integral covers the entire range of the E866 data, its value is

$$\int_{0.02}^{0.345} [\bar{d}(x) - \bar{u}(x)]dx = 0.068 \pm 0.007 \pm 0.008, \tag{6.1}$$

where the uncertainties quoted are statistical and systematic, respectively. In order to cover the full range of x, the integral of the $\bar{d} - \bar{u}$ results from E866 must be extrapolated into the unmeasured x regions. This extrapolation can be approximated by integrating $\bar{d}(x) - \bar{u}(x)$ over the needed ranges of x for various PDF parametrizations,

TABLE XI. Values for $\int \left[\bar{d}(x) - \bar{u}(x)\right] dx$ over several x ranges, evaluated at $Q = 7.35$ GeV, for various PDF parametrizations.

x range	CTEQ4M	MRS(R2)	GRV94 [21]
0.345 - 1.0	0.00192	0.00137	0.00148
0.02 - 0.345	0.0765	0.1011	0.1027
0.0 - 0.02	0.0296	0.0588	0.0584
0.0 - 1.0	0.1080	0.1612	0.1625

as shown in Table XI.

As seen in Fig. 23(a) and Table XI, the parametrization which most closely resembles the E866 results at low x is CTEQ4M. When the CTEQ4M parametrization is used to approximate the contributions to the integral from the unmeasured x regions, the integral over the full x range, as determined by E866, is found to be

$$\int_0^1 [\bar{d}(x) - \bar{u}(x)]dx = 0.100 \pm 0.007 \pm 0.017, \tag{6.2}$$

where the systematic uncertainty of 0.017 includes a contribution due to the unmeasured x regions which was estimated from the variation between CTEQ4M and MRS(R2). This extrapolation was checked by fitting the E866 results for $\bar{d} - \bar{u}$ with a smooth curve, as seen in Fig. 24, and integrating the fit over all x. The integral of the fit shown in Fig. 24 is

$$\int_0^1 0.05x^{-0.5}(1-x)^{14}(1+100x)dx \;=\; 0.097, \tag{6.3}$$

which is consistent with value quoted in Eq. 6.2.

The result for the integral given in Eq. 6.2 is slightly more than one standard deviation below the value of the same integral deduced from the NMC result. In

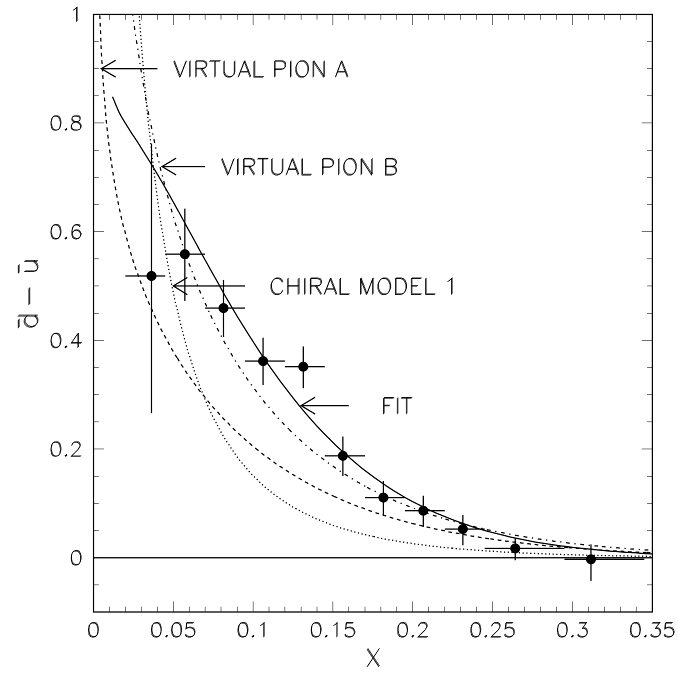

FIG. 24. Comparison of the E866 $\bar{d}(x)-\bar{u}(x)$ results with predictions of various models described in the text.

order to examine the discrepancy between the E866 and NMC results further, it is instructive to plot the difference of structure functions, $F_2^p(x) - F_2^n(x)$, in terms of the contributions from the valence and sea quark PDFs,

$$F_2^p(x) - F_2^n(x) = \frac{1}{3}x[u_v(x) - d_v(x)] + \frac{2}{3}x[\bar{u}(x) - \bar{d}(x)]. \tag{6.4}$$

In Fig. 25 the CTEQ4M and MRS(R2) parametrizations of $F_2^p(x) - F_2^n(x)$ at $Q = 2$ GeV are compared to the values measured by NMC. This figure also shows the sea quark contribution to the structure function difference as predicted by the CTEQ4M and MRS(R2) parametrizations and as measured by E866. In both of these comparisons, the parametrizations poorly describe the NMC data in the interval $0.2 < x < 0.4$, the same region where they overestimate $\bar{d}(x) - \bar{u}(x)$ as determined by E866. This points to a possible reason for the apparent difference between the E866 and

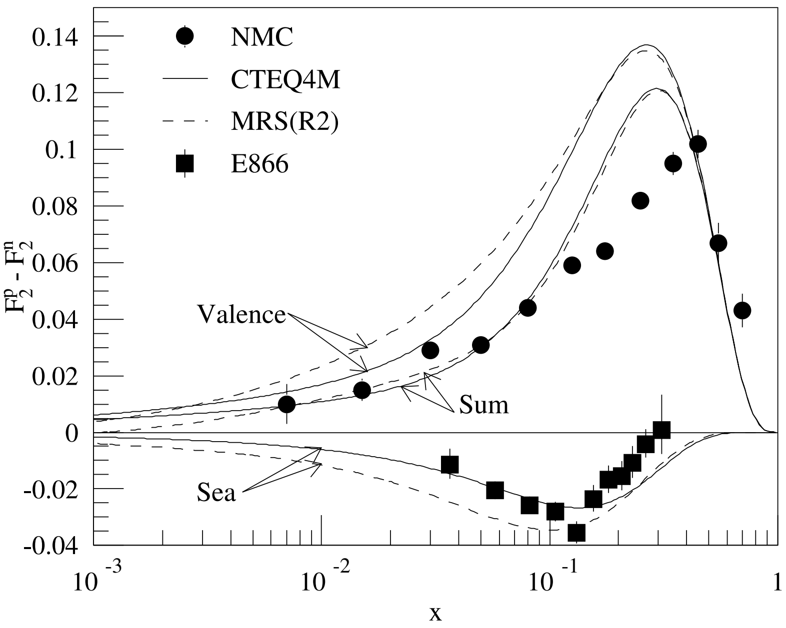

FIG. 25. $F_2^p - F_2^n$ as measured by NMC compared with predictions based on the CTEQ4M and MRS(R2) parametrizations. Also shown are the E866 results for the sea-quark contribution to $F_2^p - F_2^n$. For each prediction, the top (bottom) curve is the valence (sea) contribution and the middle curve is the sum of the two.

NMC results.

B. Nonperturbative models

Several models have been created to explain the structure and existence of a flavor asymmetric nucleon sea. The asymmetry predicted by some models is shown in Fig. 26, where they are compared to the E866 results for $\bar{d}/\bar{u}$.

Virtual meson models [7, 22, 23] describe the nonperturbative production of an asymmetric nucleon sea by expressing the nucleon wave function as a superposition of baryon and meson states. As an example, the physical proton, $|p>$, can be expressed as

$$
\begin{aligned}
|p> \;&=\; \sqrt{1-|\alpha|^2-|\beta|^2}\;|p_0> \;+\; \alpha\Big[\sqrt{\frac{2}{3}}\;|p+\pi^0> \;-\; \sqrt{\frac{1}{3}}\;|n+\pi^+>\Big] \\
&+\; \beta\Big[\sqrt{\frac{1}{2}}\;|\Delta^{++}+\pi^-> \;-\; \sqrt{\frac{1}{3}}\;|\Delta^{+}+\pi^0> \;+\; \sqrt{\frac{1}{6}}\;|\Delta^{0}+\pi^+>\Big],
\end{aligned}
\tag{6.5}
$$

where $|p_0>$ is a proton configuration with a symmetric sea which includes contributions from perturbative processes ($g \to u\bar{u}, d\bar{d}$), and $|\alpha|^2$ and $|\beta|^2$ are the probabilities that the proton is in a virtual $N+\pi$ or $\Delta+\pi$ state respectively. The predictions of two models of this type [22, 23], labeled Virtual Pion A and B, are shown in Fig. 26.

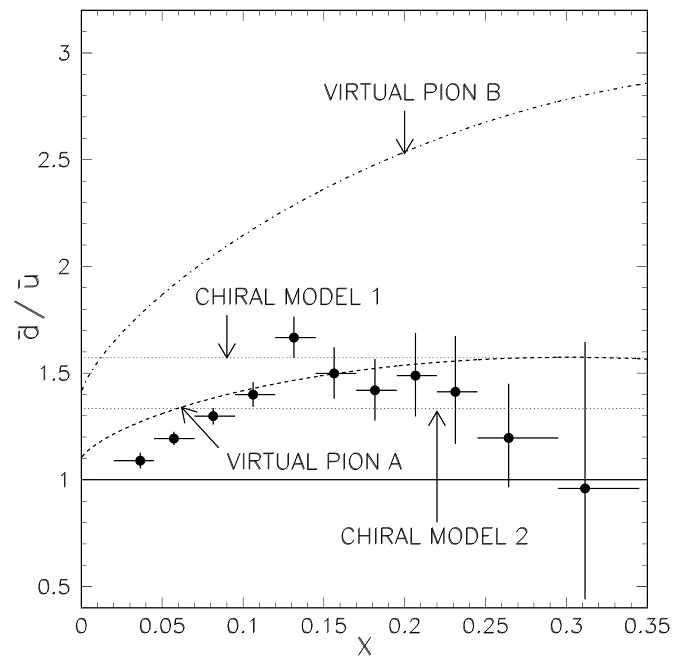

FIG. 26. Comparison of the E866 $\bar{d}(x)/\bar{u}(x)$ results with predictions of various models described in the text.

Chiral quark models [7, 24, 25, 26] also produce an asymmetric sea using non-perturbative methods. In these models, individual quarks emit and absorb virtual pseudoscalar Goldstone bosons. These bosons are usually identified as mesons with $J^P = 0^-$ (π, K, η, η'). The predictions of two models of this type [25, 26], labeled

Chiral Model 1 and 2, are also shown in Fig. 26. While chiral quark models are based on more fundamental processes than the virtual meson models, chiral models to date have not included a momentum distribution for the Goldstone bosons. Without such a distribution, the chiral quark models are unable to predict the x dependence of the $\bar{d}/\bar{u}$ asymmetry, and must resort to quoting a single average asymmetry for all x, as seen in Fig. 26.

In both types of models, an asymmetric sea is created in the proton because the production of virtual π^+ states is enhanced relative to the production of π^- states. This creates an asymmetry because the valence quarks for the π^+ are $u\bar{d}$ while for the π^- they are $d\bar{u}$. Since antiquarks in the nucleon are only formed in $q\bar{q}$ pairs, a virtual $d\bar{d}$ pair must be made to create a π^+ and a virtual $u\bar{u}$ pair must be created to form a π^-.

The models shown in Fig. 26 only describe nonperturbative methods for the creation of the nucleon sea. However, perturbative processes must also be taken into account in order for any calculation or model to describe the entire nucleon sea. The inclusion of both perturbative and nonperturbative calculations in a description of the nuclear sea is very difficult, and has not been accomplished to date with the models described above. This is because "parts" of the nucleon sea can be described by both perturbative and nonperturbative processes, so simply adding together the results from both types of calculations would result in these "parts" of the sea being calculated, or "counted", twice. The difficulty lies with determining the size and the structure of the overlap between the results of perturbative and nonperturbative calculations.

Although a quantitative calculation including both types of processes has not yet been done, it is simple to understand qualitatively what such a calculation might produce. Because perturbative processes create a symmetric sea, when these processes are added to the nonperturbative models shown above the asymmetries predicted by these models, as shown in Fig. 26, will decrease. This means that after the inclusion of perturbative processes, the Virtual Pion B model most likely will be a better fit to the E866 results than the Virtual Pion A model. It is unlikely that either chiral quark model shown in Fig. 26 will be able to accurately describe the E866 results after perturbative processes are included in their calculations of the $\bar{d}/\bar{u}$ asymmetry of the nucleon sea.

Another type of nonperturbative model has been developed which can produce a flavor asymmetry in the quark sea through the coupling of instantons to the valence quarks of the nucleon. While the instanton model found in reference [27] describes a prediction that is completely inconsistent with the E866 results, it is not known whether parameters within an instanton model can be adjusted to provide better agreement with the results.

Unlike the ratio $\bar{d}(x)/\bar{u}(x)$, a calculation of the difference $\bar{d}(x) - \bar{u}(x)$ does not require both perturbative and nonperturbative contributions to the nucleon sea in order to be able to predict the size and structure of the asymmetry. Hence, the E866 result for $\bar{d}(x) - \bar{u}(x)$, as shown in Fig. 24, can be compared directly to the models mentioned above. It is clear from this comparison that the Virtual Pion B model best describes the E866 results. The prediction from the Virtual Pion A model produces too small of an asymmetry, and the prediction from Chiral Model 1 produces an asymmetry which is too "soft" (concentrated at low x) to describe the E866 results. The authors of Chiral Model 2 did not calculate a flavor asymmetry in terms of $\bar{d}(x) - \bar{u}(x)$ for their model, but if they had, their results would most likely be similar to Chiral Model 1. The concentration of the asymmetry at low x for the $\bar{d} - \bar{u}$ predictions from chiral models arise from the pions in the model being coupled to individual valence quarks. The valence quarks on average carry less than 1/3 of the nucleon momentum, and the antiquark distributions resulting from pion production have a still smaller average momenta. This suggests that correlations between the valence quarks should be taken into account in the model.

C. Conclusion

As reported in this dissertation and in Ref. [28], the E866 experiment has measured, for the first time, the up-down flavor asymmetry in the proton sea as a function of x. The CTEQ4M and MRS(R2) PDF parametrizations are in reasonable agreement with the measured asymmetry for values of x below 0.15. At higher values of x both PDF parametrizations become completely inconsistent with the E866 results. The E866 results are now being included in the next set of global analyses done by CTEQ and MRS [29, 30]. The results of the asymmetry measurements can also be reasonably described by virtual pion models. The analysis of the remainder of the Drell-Yan data is continuing, the results of which will extend the lower limit of the x coverage to 0.015, and reduce the uncertainty of the asymmetry measurement for values of x below 0.20. Both of these improvements will also reduce the uncertainty in determining the integral of $\bar{d} - \bar{u}$ over all x. To further study the asymmetry of the nucleon sea at higher values of x, another experiment [31] is in the design and approval stage to use the 120 GeV/c proton beam from the Fermilab Main Injector for an experiment much like E866.

REFERENCES

[1] R.D. Field and R.P. Feynman, Phys. Rev. D **15**, 2590 (1977).

[2] K. Gottfried, Phys. Rev. Lett. **18**, 1174 (1967).

[3] The New Muon Collaboration, P. Amaudruz *et al.*, Phys. Rev. Lett. **66**, 2712 (1991); M. Arneodo *et al.*, Phys. Rev. D **50**, R1 (1994).

[4] B. Badelek, and J. Kwieciński, Phys. Rev. D **50**, R4 (1994).

[5] The E665 Collaboration, M. R. Adams *et al.*, Phys. Rev. Lett. **75**, 1466 (1995).

[6] C. J. Benesh and J. T. Londergan, Indiana University Report NTC-01, (nucl-th/9803017).

[7] S. Kumano, Phys. Reports (to be published), (hep-ph/9702367).

[8] S. D. Drell and T. M. Yan, Phys. Rev. Lett. **25**, 316 (1970).

[9] S. D. Ellis and W. J. Stirling, Phys. Lett. B **256**, 258 (1991).

[10] The NA51 Collaboration, A. Baldit *et al.*, Phys. Lett. B **332**, 244 (1994).

[11] The E772 Collaboration, D. M. Alde *et al.*, Phys. Rev. Lett. **64**, 2479 (1990).

[12] H. L. Lai, J. Huston, S. Kuhlmann, F. Olness, J. Owens, D. Soper, W. K. Tung, H. Weerts, Phys. Rev. D **55**, 1280 (1997).

[13] The E605 Collaboration, G. Moreno *et al.*, Phys. Rev. D **43**, 2815 (1991).

[14] C. A. Gagliardi, E. A. Hawker, R. E. Tribble, D. D. Koetke, P. M. Nord, P. L. McGaughey, C. N. Brown, Nucl. Instrum. Methods, (to be published).

[15] R. Gray and J. P. Rutherfoord, Nucl. Instrum. Methods, **A244**, 440 (1986).

[16] H. D. Glass, Ph.D. thesis, State University of New York at Stony Brook, 1985.

[17] J. A. Crittenden *et al.*, IEEE Trans. Nucl. Sci. **Ns 31**, 1028 (1984).

[18] H. M. Roder, G. E. Childs, R. D. McCarty, and P. E. Angerhofer, *Survey of the Properties of the Hydrogen Isotopes Below Their Critical Temperatures*, National Bureau of Standards Technical Note 641 (1973).

[19] D. F. Geesaman (private communication); T. R. Roberts *et al.*, Nucl. Phys. B **159**, 56 (1979); A. Breakstone *et al.*, Nucl. Phys. B **248**, 245 (1984).

[20] A. D. Martin, R. G. Roberts, and W. J. Stirling, Phys. Lett. B **387**, 419 (1996).

[21] M. Gluck, E. Reya, and A. Vogt, Z. Phys. C **67**, 433 (1995).

[22] S. Kumano, Phys. Rev. D **43**, 3067 (1991); **43**, 59 (1991); S. Kumano and J. T. Londergan, *ibid.* **44**, 717 (1991).

[23] The E866 Collaboration, J. C. Peng *et al.*, Phys. Rev. D (submitted), (hep-ph/9804288).

[24] E. J. Eichten, I. Hinchliffe, and C. Quigg, Phys. Rev. D **45**, 2269 (1992).

[25] A. Szczurek, A. J. Buchmann, and A. Faessler, J. Phys. G: Nucl. Part. Phys. **22**, 1741 (1996).

[26] T. Ohlsson and H. Snellman, http://xxx.lanl.gov/abs/hep-ph/9805309, (1998).

[27] A. E. Dorokhov and N. I. Kochelev, Phys. Lett B **259**, 335 (1991); **304**, 167 (1993).

[28] The E866 Collaboration, E. A. Hawker *et al.*, Phys. Rev. Lett. **80**, 3715 (1998). Copyright 1998 by the American Physical Society

[29] W.K. Tung, private communication.

[30] A. D. Martin, R. G. Roberts, W. J. Stirling, and R. S. Thorne, http://xxx.lanl.gov/abs/hep-ph/9803445, (1998).

[31] D. F. Geesaman *et al.*, Fermi National Accelerator Laboratory Letter of Intent P906, 1998 (unpublished).

VITA

Eric Andrew Hawker was born in St. Louis, Missouri on St. Patrick's Day in 1969. He attended Willowbrook H.S. in Villa Park, Illinois before attending the University of Illinois at Champaign/Urbana. He graduated from University of Illinois in 1991 with a B.S. in engineering physics, and proceeded to go to graduate school at Texas A&M University to study physics. He can be reached at 1906 Sprucewood, Lindenhurst, Il 60046.